Journal of Materials Research and Technology 30 (2024) 2520–2550

Contents lists available at ScienceDirect

Journal of Materials Research and Technology

journal homepage: www.elsevier.com/locate/jmrt

Metallurgical characteristics of aluminum-steel joints manufactured by rotary friction welding: A review and statistical analysis

Hossein Ghari [a], Aboozar Taherizadeh [a], Behzad Sadeghian [a,*], Behzad Sadeghi [b], Pasquale Cavaliere [b]

[a] Department of Materials Engineering, Isfahan University of Technology, Isfahan, 84156-83111, Iran
[b] Department of Innovation Engineering, University of Salento, Lecce, Italy

ARTICLE INFO

Handling editor. L Murr

Keywords:
Rotary friction welding (RFW)
Aluminum alloy-steel
Dissimilar weld
Intermetallic compounds (IMCs)
Faying surface
Interlayer
Microstructure
Mechanical properties
Optimum process parameters
Artificial neural network

ABSTRACT

Rotary friction welding (RFW) is a solid-state joining process that can be used to join different alloy systems such as aluminum-steel alloys. Rotary friction welding has become increasingly appealing for various industries due to the sustainable advantages that it offers, including overall cost reduction, weight minimization, and unique properties. However, the formation of brittle intermetallic compounds (IMCs) at the interface can be a challenge in the welding process of aluminum-steel alloys. This paper reviews the metallurgical characteristics of aluminum-steel alloy joints manufactured by rotary friction welding. The different types of intermetallic compounds that can form at the interface, as well as the factors that affect their formation, are discussed. The effects of rotary friction welding parameters on the microstructure and mechanical properties of the joints are also presented. Specifically, minimizing interfacial reaction layers via post-weld heat treatment and controlling the heat input during the process is crucial to suppressing the formation of intermetallic compounds. This study employed artificial intelligence modeling, specifically the artificial neural network - multilayer perceptron, to investigate the effect of various parameters on the ultimate properties of the parts welded together. Overall, this paper provides an excellent resource for industries looking to embrace rotary friction welding to tackle the challenge of dissimilar Al-steel joining.

1. Introduction

Welding is one of the most frequently used production techniques. In some circumstances, dissimilar metal joints are required due to design constraints, such as the system's overall cost when materials cost is taken into account, the structure's overall weight when material density is taken into account, and the requirement for parts with various mechanical properties. As a result, there is a need for dissimilar metal joints in several industrial applications where it is common to combine the special qualities of two welding components for improved performance [1–6].

The hybrid structure built on a multi-material design may completely utilize the benefits each metal has to offer, adjusting to the challenging service circumstances. The use of hybrid welded joints of aluminum alloys to steel has been broadly used in industries due to the advantages of weight reduction, performance enhancement, and reduced energy consumption [7]. Aluminum/stainless steel multi-material systems are of significant interest for their high strength-to-weight ratio and corrosion resistance in many application areas such as automobiles, airplanes, high vacuum chambers, cryogenic pressure vessels, windscreen frames, bumper reinforcement, center pillars, floor pan, marine industries, and pipes of liquid fuel tanks in Satellite Space Vehicle [1,8–12].

However, the process of joining aluminum and steel through fusion welding presents several challenges that must be carefully considered. One key factor is the high thermal conductivity of aluminum, which can lead to rapid heat dissipation during welding processes such as TIG. This can result in low heat utilization, necessitating increased heat input and potentially causing incomplete penetration and non-fusion defects [1,13–16]. Another challenge is the low solid solubility of iron (Fe) in aluminum (Al), which can lead to solidification and liquation cracks, as well as porosity formation during welding [10,11,17–20]. Additionally, the significantly larger coefficient of thermal expansion and different melting temperatures between aluminum and steel can contribute to distortion and high residual stresses in the welded joint [10,11,18–20].

* Corresponding author.
E-mail addresses: a.taheri@cc.iut.ac.ir (H. Ghari), h.tehrani@alumni.iut.ac.ir (A. Taherizadeh), behzadsadeghian91@gmail.com (B. Sadeghian), behzad.sadeghi@unisalento.it (B. Sadeghi), pasquale.cavaliere@unisalento.it (P. Cavaliere).

https://doi.org/10.1016/j.jmrt.2024.03.089
Received 25 January 2024; Received in revised form 13 March 2024; Accepted 14 March 2024
Available online 7 April 2024

Furthermore, the formation of IMCs, such as FeAl2, FeAl3, and Fe2Al5, can increase joint brittleness and hardness, leading to crack formation and residual stress issues [17,21]. The formation of a tenacious Al2O3 oxide film on the aluminum surface during welding can also create challenges by hindering proper bonding, leading to slag inclusions and embrittlement, ultimately degrading joint performance. In addition, the high welding temperatures can generate hydrogen atoms that enter the molten metal, forming pores within the weld [13]. Moreover, specific aluminum alloys, such as the 2xxx series, present inherent challenges for welding using traditional techniques. They require specialized expertise and are susceptible to softening and heat-affected zone formation due to dissolution/over-aging [22]. Therefore, the connection might collapse during fusion welding, maintenance, or shortly thereafter. To promote the joining of dissimilar metals and prevent the deterioration of the joints' mechanical and metallurgical characteristics, an efficient and reliable welding procedure is needed.

Hence, solid state-based welding procedures are suggested for parts involving dissimilar materials. A solid-state processing approach is used to operate friction-based welding techniques, which use compressive force and frictional heat as controlling variables to produce strong metallurgical welds. Al-steel combinations are therefore effectively welded using rotary friction welding and the defects mentioned above may all be prevented using less heat and a shorter amount of welding time [19,20,23–26]. For instance, laser welding requires filler metal and shielding gas, as well as expensive equipment [27–29], and is prone to solidification cracking [30], whereas brazing requires torch position adjustment and changing the chemical composition of the filler wire in the aluminum-steel connection [31]. However, these limitations are eliminated by rotating friction welding.

While rotary friction welding overcomes the limitations of fusion welding, distinct interfacial microstructures, such as amorphous phases and crystalline IMCs, often form due to the combined effects of thermal-mechanical coupling during the friction welding process [32]. To control and reduce the amount of IMCs, various useful methods have been developed, including the use of interlayer and adjustment of process parameters. Furthermore, the finite element method (FEM) is a developed field that is becoming increasingly important for the design and optimization of welding processes. Gill et al. [33] reviewed the effects of different welding parameters with FEM for some of the RFW of Al-St joints.

A considerable number of review articles have been published in the last decade on fusion welding of aluminum-steel [27,28,31,34,35], solid-state welding of aluminum-steel [1,15,36,37] and friction stir welding of aluminum-steel [17,21,38,39]. However, none of them have been specialized and focused on steel-aluminum rotary friction welding in details. In recent years, there has been an extensive amount of investigation into steel-aluminum rotary friction welding. Hence, the fundamentals of rotary friction welding processes are reviewed, with particular emphasis on the bonding mechanisms, microstructure development at the weldment, advantages, challenges, and solutions for obtaining proper welds for different aluminum grades. Additionally, methods for controlling intermetallic compounds at the joint interface are discussed. Specifically, the effect of process variables on the development of microstructure and mechanical properties of distinct dissimilar aluminum-steel joints is classified independently. In the Appendix, an artificial neural network-multilayer perceptron, as an artificial intelligence analysis, was utilized to investigate the impact of various parameters on the ultimate properties of the weldment. This review may provide guidelines and motivation for future research in this field.

2. Rotary friction welding

A non-traditional form of welding called friction welding (FRW) allows for both similar and dissimilar pairings since the joining takes place while the structure is still solid. In rotary friction welding (RFW) axial forging pressure is applied after one workpiece is constantly pushed against another at a specific rotating speed, generating frictional heat and softening the workpiece. When they are plasticized, the interface material is forced out of the joint's borders, leaving clean material from each component along the initial interface. Recrystallization is hence accomplished by thermo-mechanical processes. The main benefit of RFW is that no liquid metal is produced, and the weld that is being created is solid. Since the 1940s, rotational friction welding has been employed commercially [33,40–43].

2.1. Types of RFW

Probably, the most typical FRW process variant is RFW. Its fundamental idea is demonstrated in Fig. 1a, where a static component is compelled to push against a spinning workpiece while being exposed to normal pressure. Direct-drive friction welding, also known as continuous-drive friction welding (CDFW), and inertia friction welding (IFW), also termed inertia-drive or inertia welding) are the two method variations. The manner of providing energy to the welding contact is the main distinction between these two techniques. The spinning workpiece in CDFW is coupled to motor-driven equipment that maintains a consistent rotation speed during the welding operation (Fig. 1b). The procedure continues up to the application of a braking force or the production of axial shortening, commonly known as burn-off or upset [42,44].

In IFW, a flywheel is attached to the spinning workpiece. It is driven to the proper rotating speed, then the drive motor is cut off, and welding may then occur. Here, the flywheel's rotation provides the kinetic energy that is converted to frictional heat and used to weld the junction. The flywheel's speed progressively drops until it reaches zero (Fig. 1c) [42,44]. IFW occasionally forgoes the further deployment of a forging force. However, a forging stage is necessary for the vast proportion of applications. It must be noted that Fig. 1c's definition of a single-stage and two-stage process is ambiguous and only applies to RFW. Although friction pressure can be delivered in one or more stages, it can also be applied continuously. Additionally, forging is done just after the welding process without changing the steps or physical processes of RFW. These procedures include single-stage pressure and two-stage pressure [44].

RFW typically consists of two stages. The friction stage, during which the material is heated and the required upset is created, and the forging stage, during which the weld is formed (Fig. 1b and c). IFW can meet substantially greater input energy standards than CDFW due to the variety of energy input sources. Because of this, CDFW is used by the automobile industry and IFW by aircraft engine manufacturers [44]. In recent decades, dissimilar metals such as aluminum and steel have been used in approximately 8.6% and 7.7% of published research results on CDFW and IFW, respectively [44,45].

2.2. Interface evolutions and bonding mechanisms

The mating surface rubbing mechanism has a molecular and mechanical basis. The mechanical action is produced by the pieces rubbing against one another, whereas the molecular action is caused by the attraction of two portions to one another. The two contact methods that contribute to friction welding are solid-state diffusion and mechanical mixing (asperities interlocking) [42,46–49]. Despite what has been stated, friction welding joints tend to be stickier than diffusional ones [50]. Fig. 2 illustrates how frictional heating causes asperities on the faying surfaces to interlock and rupture, and also how RFW creates the bond. Even though rotary friction welding has a quick heating time, Gelman proposed that the bond occurs during cooling because of the lengthy cooling time [42].

To better understand the process evolutions, as seen in Fig. 3, the RFW process may be split into four stages [24,51].

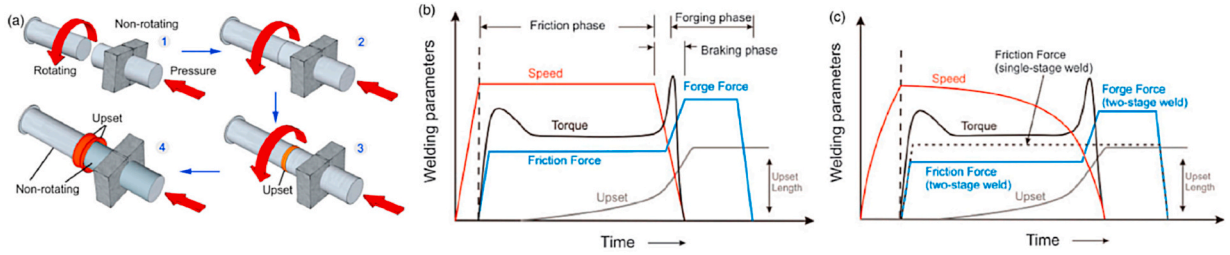

Fig. 1. Schematic of (a) the RFW process; (b) process phases of CDFW; and (c) IFW [44].

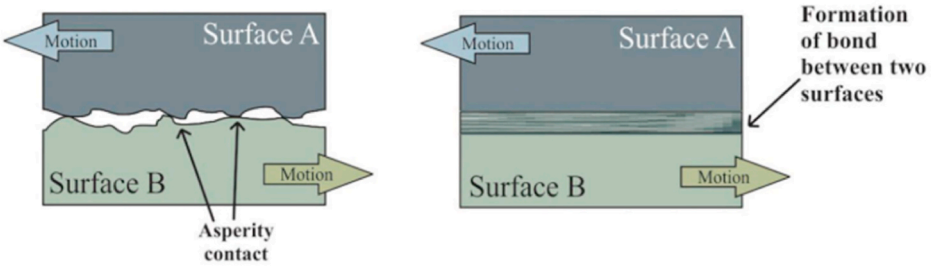

Fig. 2. Formation of the bond by FRW [41].

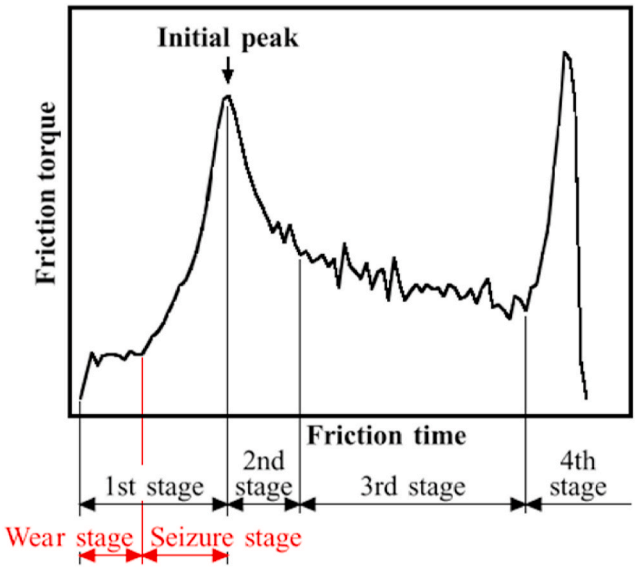

Fig. 3. Definition of stages on the friction torque curve and division of a part in the first stage [51].

1) Initial friction stage: during this stage, heat is generated by friction when the rotating and moving ends contact one another. As a consequence, the metal at the interface on both sides transforms from an elastoplastic to a viscoplastic state, and the friction at the interface progressively transforms from sliding friction to adhesive friction. This causes a substantial rise in friction torque to the initial peak torque.
2) Quasi-steady friction stage: at this stage, most of the heat generation is caused by plastic deformation, and the metals at the interface all undergo a viscoplastic transformation, which causes the friction torque to begin decreasing. The viscoplastic metal is extruded to generate flash because its yield strength is lower than the friction pressure exerted at the contact.
3) The steady state is the third stage.
4) Forging stage: the motor begins to brake, the friction torque rapidly increases to the last peak torque, and the viscoplastic metal at the interface is extruded to create a flash in the fourth step, which is known as forging. When the motor stops spinning, the torque immediately decreases to terminate the welding. The Evolution developments at the interface are summarized in Table 1.

2.3. IMCs formation and control approaches

Fe has limited solid solubility in Al, and at room temperature, this solubility is almost negligible. According to Fig. 4, the solid solubility range of Fe in Al is 0.01–0.022% at temperatures between 225 and 600 °C. The Fe–Al phase diagram (Fig. 4) depicts two types of IMCs: Fe-rich phases (Fe_3Al and FeAl) and Al-rich phases (Fe_2Al_5, $FeAl_2$ and $FeAl_3$). Table 2 summarizes the IMCs of the Al–Fe system in terms of their crystal structures and hardness. Heat input, which is controlled by the welding process variables and the chemical composition of the materials, determines the type, size, and total amount of IMC formation [12,17,25,26,52]. The thermodynamic aspect, lower Gibbs free energy (ΔG) phases have a higher probability of forming. The sequence of the Gibbs free energy for several Fe–Al IMCs is as follows [53,54]:

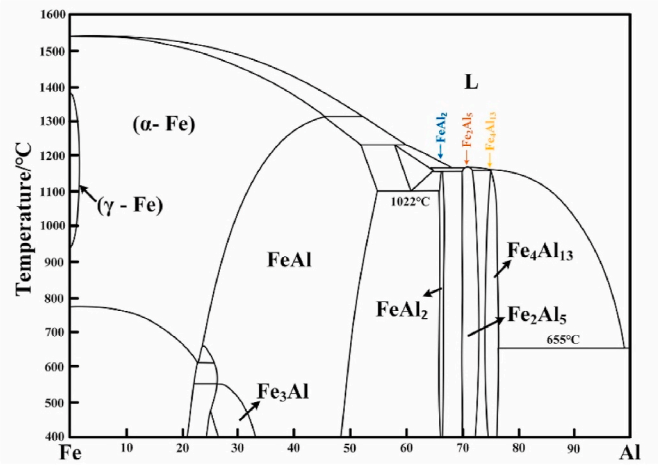

Fig. 4. The Al–Fe phase diagram [52].

Table 1
The evolution of the friction torque changing procedure at the interface of RFW [24,51,55,56].

Friction torque changing procedure		Evolution developments at the interface
1- First stage: Heat-up stage or rising friction torque (indented)	1-1 Wear stage: (a) Abrasive (b) Adhesion (Stick)/Slide	dry friction, temporary adhesion bonding, and junction (adhesion friction surface/sliding friction surface)
	1-2 Seizure stage	faying surfaces contact, interlocking and breaking of asperities at the faying surfaces by frictional heating, rising atomic diffusion by increasing frictional heating, initiation of the intermetallic compounds
2- Second stage: Decreasing friction torque (Quasi-steady state)		rising friction heating, decrease in the flow stress, transformation of oxides and contaminations at the faying surfaces plastically flows outwards to form the flash, initiation of burn-off
3- Third stage: Burn-off stage or steady (equilibrium) state		balance between work hardening and work softening, growing plasticized layer
4- Fourth stage: Rising friction torque or forging stage		applying a high compressive force, formation of dynamic recrystallized structure

Table 2
Summary of crystal structure and hardness of different IMCs of the Al–Fe system [1,39,57].

Intermetallic compound	Al percent's (at. %)	Crystal structure	Vickers hardness
Fe_3Al	25	Ordered BCC/DO_3	330–368
FeAl	50	BCC	470–667
Fe_2Al_3	63	Complex Cubic	650
$FeAl_2$	66–67	Triclinic/Rhombohedric	1000–1070
Fe_2Al_5	69.7–73.2	BCC orthorhombic	1000–1158
$FeAl_3$	74–76	Highly complex monoclinic BCC	772–1017

$$\Delta G^0(Fe_2Al_5) < \Delta G^0(FeAl_3 < \Delta G^0(FeAl_2) < \Delta G^0(FeAl) < 0 < \Delta G^0(Fe_3Al) \quad (1)$$

Fe_2Al_5, Fe_4Al_{13}, and $FeAl_3$, which have lower ΔG, are considered the major compound layers that form at the weld interface, based on the ΔG of Fe–Al intermetallic compounds at various temperatures shown in Fig. 5 [12].

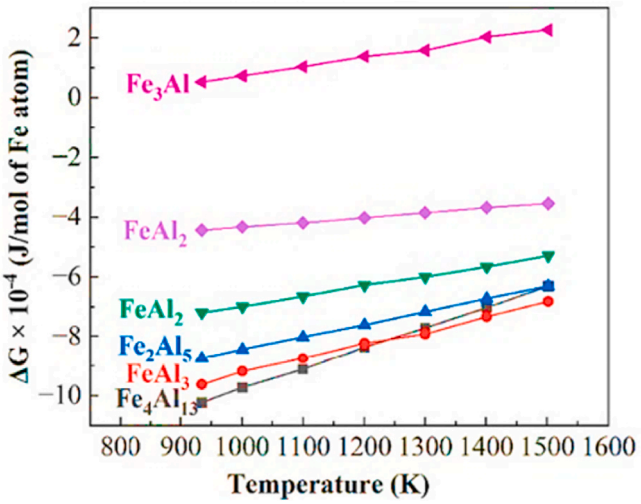

Fig. 5. ΔG of Fe–Al IMCs at different temperatures [12].

At a temperature of 623 K (350 °C), Fig. 6 illustrates the Gibbs free energy and formation enthalpy of Fe–Al phases in the form of amorphous and IMC with various compositions. For meaningful comparison, Fig. 6 also indicates the composition variety of common IMC phases mentioned in the research, such as Fe_2Al_5 and Fe_4Al_{13}. When two phases have comparable element compositions, as illustrated in Fig. 6, the amorphous phase has a greater formation enthalpy and Gibbs free energy than the IMC of the Fe–Al phase, indicating that the Fe–Al IMC is thermodynamically preferred to form at the Fe–Al interface [25].

Fig. 7 depicts a schematic representation of the Fe–Al IMC formation mechanism. This procedure may be divided into four steps: (i) Metal-to-metal contact causes Al and Fe atoms to diffuse toward the interface at a slow inter-diffusion rate (Fig. 7a) [12,53] and the amorphous phase is formed in the first stage [39]. (ii) The creation of discontinuous Fe_2Al_5 IMCs is caused by an acceleration of the rate as the Fe atoms reach a saturation concentration in the Al matrix. At that stage, the Fe_4Al_{13} IMC starts to nucleate because it has the lowest necessary free energy of formation. Fe_2Al_5 has a higher diffusion rate than the other Fe–Al IMCs, which leads to the formation of discontinuous Fe_2Al_5 IMCs (Fig. 7b). (iii) As the interface welding energy increases, discontinuous Fe_2Al_5 grains grow quickly and eventually merge to form a continuous structure. Due to vacancies in the Fe_2Al_5 crystal structure, the Fe_2Al_5 grows vertically along the Al/steel contact, forming coarse columnar crystals (Fig. 7c) [12,53]. Also, the Fe_2Al_5 to Al–Fe phase transition occurs assisted by a greater heat cycle [39]. (iv) At the end of the welding process, needle-like Fe_4Al_{13} IMCs form near the Fe_2Al_5 layer (Fig. 7d) [12,53]. Additionally, it was observed that an extended heat cycle with a greater peak temperature led to the creation of $AlFe_3$ after the production of Fe_4Al_{13} [39].

Beygi et al. [38] reported that silicon (Si) in aluminum alloys has the strongest effect on slowing down the growth of iron-aluminum intermetallic compounds (IMCs). In aluminum alloys containing Si as a solid solution element, the IMC layer is thinner than 4 μm. Additionally, nickel (Ni) and chromium (Cr) in stainless steel also reduce the thickness of IMCs by hindering diffusion and potentially strengthening the IMCs.

Two types of IMC morphologies may be distinguished at the welding interface. The first IMC is tongue-like on the steel side such as Fe_2Al_5, and the second is needle-like near the aluminum side such as Fe_4Al_{13} [12,34,53]. Furthermore, Fe_2Al_5 is the main phase that affects the quality of welded joints [34].

During friction welding, the proper flash of Al is essential because the link between Al and steel typically forms in the outside surface area before moving inside toward its center. As a result, as illustrated in Fig. 8, the generation of the IMC layer is observed to be thicker in the outside zone and thinner in the middle [1,6].

Assuming diffusion process control, the following parabolic equations may be used to determine the reaction layer thickness and evolution of Fe–Al IMCs:

$$X = \sqrt{t}\left(K_0 \exp\left(-\frac{Q}{RT}\right)\right) \quad (2)$$

where X is the reaction layer thickness (mm), t is the diffusion time (s), K_0 is a constant, Q is the layer growth activation energy (J), R is the gas constant, and T is the absolute temperature (K). If the IMC layer's thickness (X) and diffusion time (t) satisfy the parabolic law, bulk diffusion of Fe and Al drives the IMC layer's development [1,10].

The interfacial layer of the Al/steel weld may thus easily produce brittle intermetallic compounds that cause the formation of cracks and generation of welding residual stress. In the majority of literature research of Al-steel friction welding, several IMC phases of FeAl, Fe_2Al_5, and $FeAl_3$ are documented [19,26,58,59]. The creation of various IMCs is mostly attributed to the solid-state diffusion and mechanical intermixing mechanisms [1].

Controlling the thickness of the IMC layer is essential when welding dissimilar materials since IMC development can be detrimental to

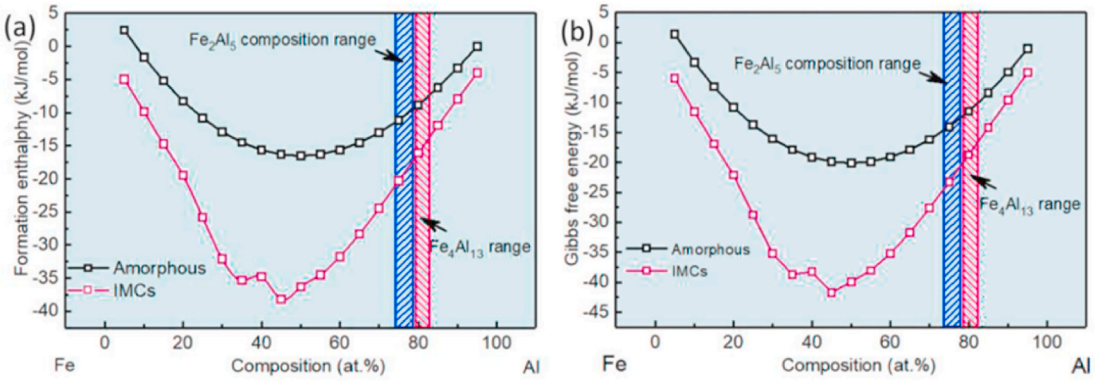

Fig. 6. Formation (a) enthalpy and (b) Gibbs free energy of Fe–Al amorphous phase and IMCs [25].

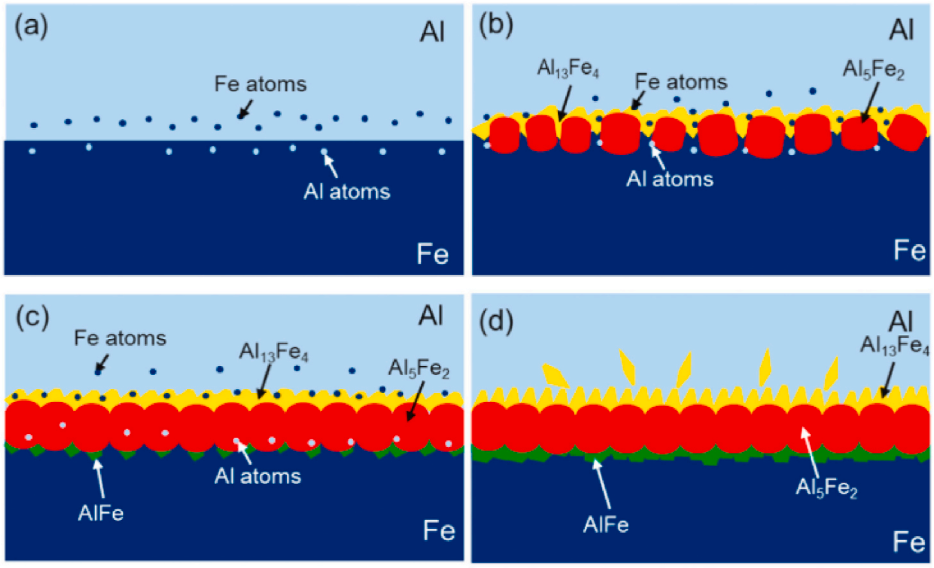

Fig. 7. The mechanism of Fe–Al IMC formation in different stages: (a) stage 1, (b) stage 2, (c) stage 3, (d) stage 4 [53].

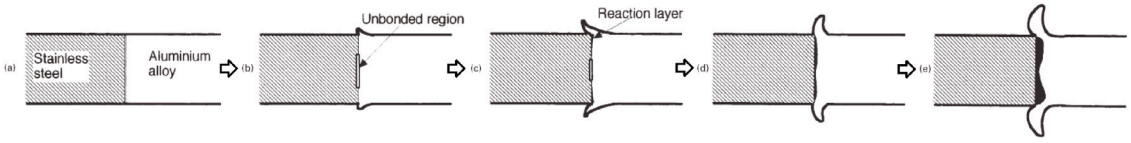

Fig. 8. Reaction layer formation steps in dissimilar Al-steel friction welding [6].

welded joints. Several methods can be used if the thickness exceeds a certain value [12]. Some have been working to decrease the formation of intermetallic compound layers in recent years. It is possible to produce excellent joints without noticeable intermetallic compound layers by.

1) Adjusting the process parameters: A significant quantity of experimental validations is necessary to establish suitable welding parameters in the initial phases of the experiment [12,24]. Rotational speed, upset pressure, upset time, friction pressure, and friction time are essential friction welding factors [1,36]. According to the chemical composition of the welding materials and the varying range of other process variables, increasing friction time causes an increase in interface temperature, a change in the residual stress in the weldment, strength properties, and IMC film thickness [9,18]. In general, friction welding parameters that control heat input determine the type, size, and amount of IMCs. So, it is advised to optimize welding parameters to perform joints with less heat input [1,60,61]. Diffusion is responsible for growth, as evidenced by the linear relation between the intermetallic interlayer thickness and the square root of friction time [62]. Even though, process parameters frequently need to work together and several experimental verifications are necessary to get suitable welding parameters in the initial stages of the experiment, high-quality welds without evident IMC layers may be achieved by optimizing the process parameters [24].
2) Pre-weld heating: Because of the higher atom mobility, preheat treatment encourages the formation of the crystalline layers while inhibiting the amorphous layer. Preheating enhances local interfacial interaction strength by minimizing unbounded area whilst retaining excellent welding quality [25].
3) Modifying faying surfaces: Faying surfaces can be modified by being machined into different forms, such as a V or U with various taper

angles, which offers a route for IMCs to flee with the flow of the material [9,63,64].

4) Post-weld heat treatment: Even though some researchers have used post-weld heat treatment to reach the target of homogenizing the contact microstructure and mechanical characteristics, the issue of heterogeneity in the radius axis cannot be adequately resolved [24, 60].
5) Employing various interlayers: for example, alloy, metal, and nano-structure interlayers can be used to increase the microstructure and mechanical characteristics heterogeneity in the radial axis [24]. Welding a layer connecting two components requires the employment of the following distinct techniques: A two-step welding process that uses a third metal, called an interlayer metal, to join two others. In this process, the first metal is welded to the interlayer, and then the interlayer metal is cut to a specific length and welded to the second metal [65,66], electroplated interlayer coating on one of the components [67–71], placing interlayer material in the shape of a coin into the base metals drilled hole [72,73], sheet plate interlayer [74,75], simultaneous joining in a one-step by attached interlayer to the center gear through drill holes [23], using insert powdered metal [76], and brush plating [24]. These interlayer materials serve two purposes: (i) acting as a diffusion obstacle to prevent the metallurgical incompatibility-related creation of brittle compounds; and (ii) lowering the friction coefficient to maintain a lower interface temperature and prevent substantial interaction, which can result in the brittle compound nucleation [77].

3. Metallurgical characteristics of Al alloy-steel joints

Numerous efforts have been made to weld different types of aluminum alloys with steel alloys. Currently, RFW has welded several types of Al alloys with steel, including the 1xxx (pure Al), 2xxx (Al–Cu), 5xxx (Al–Mg), 6xxx (Al–Si), and 7xxx (Al–Zn) series, in which the weldability of Al alloy to steel was typically examined. The scientists concluded that these three series of Al alloys—1xxx, 5xxx, and 6xxx—were moderately weldable to steel using FRW [78].

Al–Si is most frequently utilized as the aluminum component, and ferritic carbon steels or austenitic stainless steels are most typically used as the steel portion. An Al_2O_3 film on the Al weld part initially serves as an obstacle to forming a connection, which is a characteristic of all Al alloys. High rotating speeds and pressures, however, cause this layer to break, resulting in an oxide-free aluminum part surface that could be welded. However, microscopic studies can reveal the existence of Al_2O_3 layers. The strength of the weldment is adversely affected by defects in the Al/steel bonding, such as fractures, porosity, IMC phases, detached regions, distortions, etc. Welding parameters that are appropriately specified determine the weld's quality [62]. Results in commercially available worked aluminum alloy types and carbon steel demonstrate that [79].

1. Friction welding of the AA1050, AA5052, and 6000 series alloys results in acceptable joints being generated across a reasonably wide variety of friction welding parameters, excellent friction weldability, and an optimum joint performance of more than 75%. Since AA5052 and 6000 series alloys have low amounts of magnesium, which prevents welding when subjected to a higher percentage, they have proper friction weldability, similar to pure aluminum
2. Despite having a reasonably broad range of friction welding parameters over which acceptable joints may be generated, the maximum connection performance for A5056 is approximately 50% when it is friction welded. Due to the high magnesium concentration of A5056, extensive, brittle IMC layers occur, which results in considerably less favorable friction weldability
3. During friction welding of 2000 series alloys and A7075, there is a short range of friction welding parameters over which moderately strong bond strength may be achieved, the highest joint performance is in the range of 20–40%, and poor friction weldability is generated. Weak friction weldability of these alloys arises from the formation of brittle Cu–Al and Al–Cu–Fe IMC layers at the weld interface
4. When solid rod joints and pipe joints are compared in terms of weld performance, solid rod joints come out on top.

In the next sections joining of aluminum series to steel alloys is discussed to clarify more details.

3.1. Al 1xxx series to steel joint

Commercially available aluminum was friction-welded to stainless steel, and the aluminum's microstructures adjacent to the weld boundary were examined by TEM. Following the upset stage, grain growth took place during air cooling. Due to the temperature differences, the grain size was higher in the center than in the exterior. In Fig. 9, the resultant microstructure is seen close to the weld boundary (x = 150 μm). Although recrystallized grains can't be seen, the microstructure of the material contains a large number of hot deformed cells that were developed during the friction stage. Dynamic recrystallization therefore began throughout the upset stage [80].

The weld should be produced without greater upset pressure and with a suitable friction time where the friction force achieves the initial maximum to improve the joint performance of CP-Al-LCS welds and fracture on the CP-Al side. In other words, as upset pressure increased, the weld performance declined and at 0.9 s of friction time, all joints on the CP-Al side cracked. When the compressive stress was greater than the CP-Al base metal's yield point, the tensile strength of the metal decreased by increasing applied pressure at any temperature. As a result, the Bauschinger effect caused the tensile strength of the CP-Al base metal to drop, resulting in the joint did not reach 100% weld performance. By passing time, CP-Al transferred to the low carbon steel side's half-radius area of the weld interface before moving toward the whole weld zone (Fig. 10) [81].

Kimura et al. [82] reported that the tensile strength of friction-welded joints between commercially pure aluminum (AA1070) and low carbon steel (LCS) decreased as the forge pressure increased. The shape of the weld faying surface and tempering condition of the AA1070 side were altered to compensate for the decrease in tensile strength.

When welding 1060 pure aluminum rod to Q235 low-carbon steel, the Ag interlayer forms Ag_2Al, Ag_3Al, and Fe_2Al, Fe_4Al_{13} IMCs close to the edge of the weld, but does not completely address the heterogeneity of interface element distribution and mechanical characteristics at the varied radius of weld interface [24]. Also, five different conical Q235 low-carbon steel rod types to 1060 aluminum rods were welded using CDFW at lengths of 5, 10, 15, 20, and 25. The conical end face's increased tilt angle caused the corona bonding. A decrease in friction heat and an increase in tangential stress also cause dynamic recrystallization of the joint's friction contact to shift from the exterior to the interior. Consequently, the corona bonds shrank. The IMC thickness at the 15° tilt angle connections had the smallest variation throughout the radius and was dispersed in the shape of a "rodent" on the aluminum side, reaching a maximum thickness of 1.05 m at 3/5R and a mean thickness of around 0.85 m. The tensile strength and thickness of IMC layers at various contact radii are shown in Fig. 11a, b [45]. Additionally, Vee-joint welds of AA 1050-AISI 1050 CS have been shown to have greater strength than round and plain joint welds, according to Reddy et al. [83].

The CP-Al-SS304 welded joints should be produced with a high forge pressure of 150 MPa and with the appropriate friction time so that the temperature on the weld contact reaches around 573 K or higher to get a good joint with greater joint performance and bending ductility. The weld exhibited a bending ductility of 90° in a specific direction and no crack at the weld zone as they were formed at a friction time of 1.0 s with an upset pressure of 150 MPa. This joint was similarly 90° bending

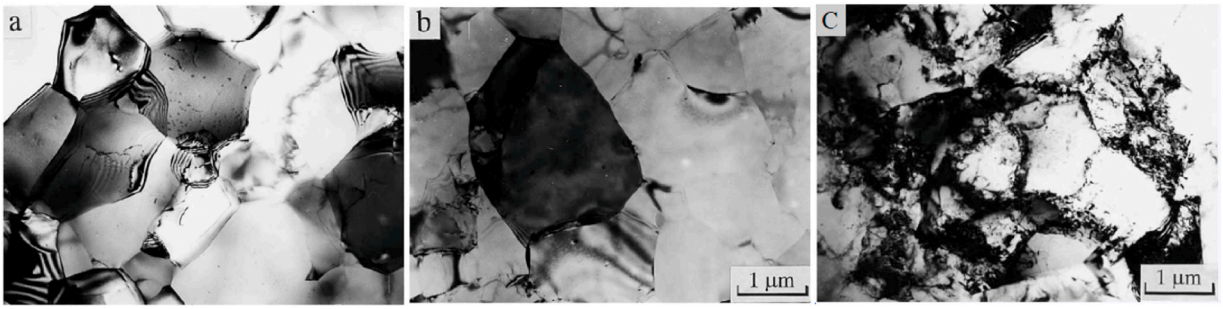

Fig. 9. Effect of (a) water cooling (b) air cooling after upset process on dynamic recrystallization (c) microstructure of Al at x = 150 μm without upset process, i.e. water cooled after friction stage (TEM) [80].

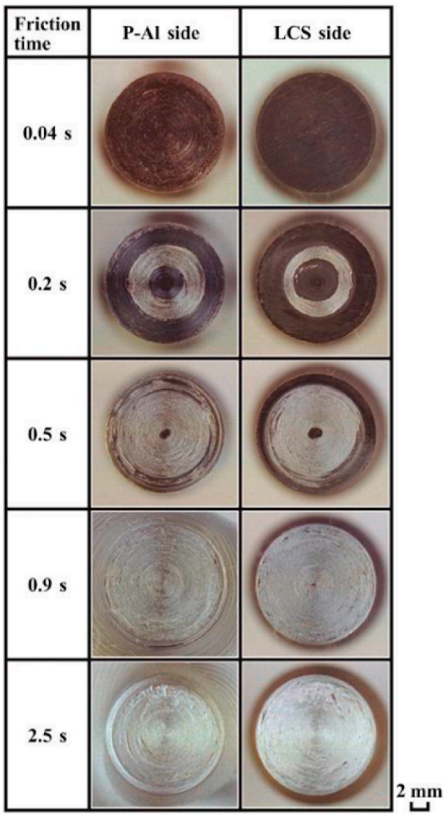

Fig. 10. Appearances of weld interface after welding [81].

ductile in the other direction without a crack (Fig. 12). Because of the discrepancy in the anisotropic characteristics and the decrease in the tensile strength of the CP-Al base metal brought on by the Bauschinger effect, the joint did not have 100% performance [84]. It was observed that the radial axis temperature at the joints between AA1070 and SS 304 had values that were nearly consistent regardless of the radial locations. However, when friction duration increases, the contact temperature rises [85]. Additionally, martensite instead of austenite replaced the previous structure of the stainless steel's faying surface. As a result, the stainless steel was toughened close to the AA 1050-SS 304 weld contact [5].

To look into how oxidation affected the bonding of CP-Al/IF steel and CP-Al/AISI 304 steel joints, Yilmaz et al. [62] evaluated the influence of friction times in two distinct air and argon atmospheres.

In Fig. 13, it can be observed that the interfacial thickness rises as the friction duration increases. The interfacial thickness in Al/IF steel is almost twice as great as that in Al/stainless steel for the specimens generated under an Argon atmosphere with similar friction durations. The linear relationship between the interfacial thickness and the square root of the friction duration suggests that diffusion is responsible for the interface's development. Being welded in an Argon atmosphere, the interfacial thickness in the Al/IF steel part increases quickly [62].

The interfacial development of a porous oxide during preheating and friction in a regular environment reduces the weld's strength. A strong interface can form during welding in an Argon environment. However, in the current investigation, the existence of oxides could not be completely ruled out. In contrast, whereas chromium oxide binds tightly to the steel matrix in Al/stainless steel samples, iron oxide in Al/IF steel components is nearly fully removed from the interfacial area into the plastically deformed Al region. The contact area cannot easily be removed from chromium oxide. As a result, only a few sites where the chromium oxide is fractured enable the formation of an interfacial phase, and an interlayer phase can only occur in those locations where the chromium oxide detaches from the interface [62].

3.2. Al 2xxx series to steel joint

Because of their high strength and widespread use in aerospace industries, 2xxx (Al–Cu) series Al alloys are very unique from those of other series Al alloys. This difference could have a significant impact on the metallurgical response and subsequent mechanical behavior of Al alloy/steel FRW joints [78].

Al_2Cu is less likely to develop than Fe–Al IMCs because the typical Gibbs free energy of Fe–Al IMCs is much less than that of Al_2Cu. Yet, there are hardly any Fe–Al IMCs in the IMCs layer near the friction contact. As a result, inter-diffusion between various elements could not be the cause of the Al–Cu IMCs' production in the current case. The thermo-mechanical coupling effect would cause Al_2Cu particles in Al alloy to break and partially dissolve, as seen in Fig. 14. The fragmented Al_2Cu particles swiftly reach the undulating interface by the plastic flow of Al alloy under friction stress and accumulate in special areas, functioning as nucleated particles. The precipitation of the Al_2Cu phase from the Al alloy and the agglomeration of Al_2Cu particles causes the IMCs layer to grow rapidly after that. A thicker Al_2Cu IMC layer under a high heat input, however, can experience cracks more quickly. Thus, by managing the welding parameters, the significant development of the Al_2Cu IMC layer might be prevented [78].

Dang et al. [86] found that the thickness of the Fe–Al IMC layer was closely related to the thermo-mechanical distribution at the interface. In the flat surface joint, the Fe–Al IMC layer was thicker in the 1/2 radius zone than in the center zone due to the higher temperature and plastic flow of the Al alloy. However, in the tapering surface joint, the Fe–Al IMC layer was thinner in the center zone due to the higher peak temperature, which caused a large number of Al_2Cu particles to break and partially dissolve during the welding process. The authors concluded that the bonding strength of the welded joints was affected by the thickness and type of IMC layers formed at the friction interface. The joints with a thicker Fe–Al IMC layer in the center zone had higher tensile strength than the joints with a thinner Fe–Al IMC layer or a

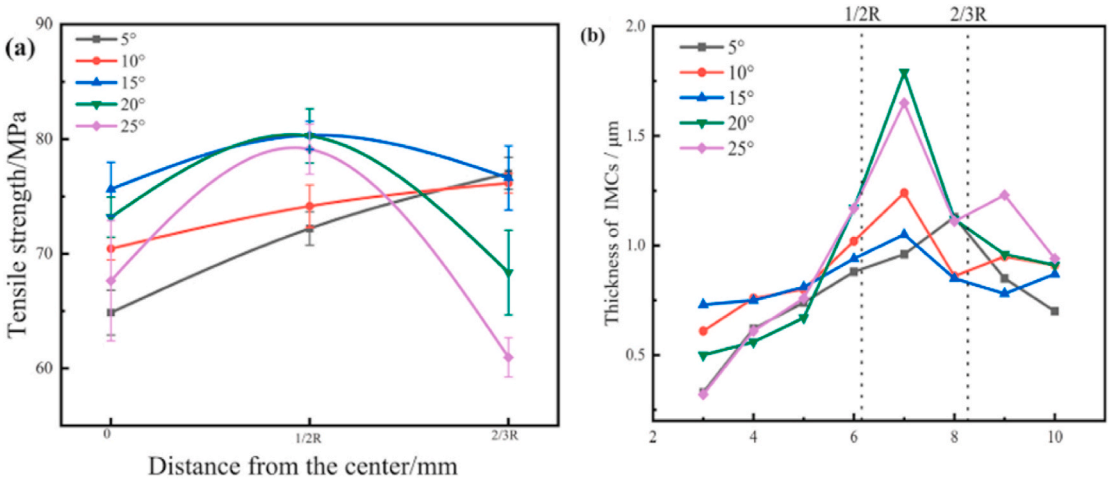

Fig. 11. (a) Tensile strength of slices (b) the distribution of IMCs layer thickness at the interface with radius for five types of conical joints [45].

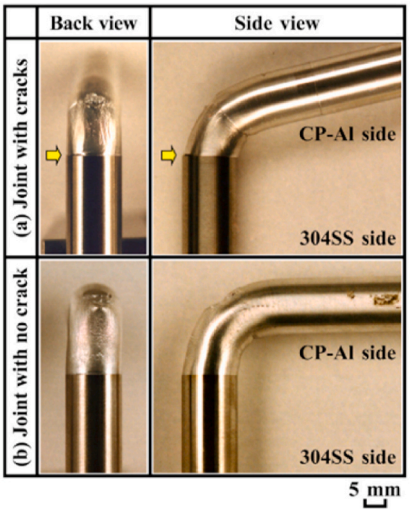

Fig. 12. Appearances of joint bending tested specimens by reverse direction bending test: forge pressure of 150 MPa [84].

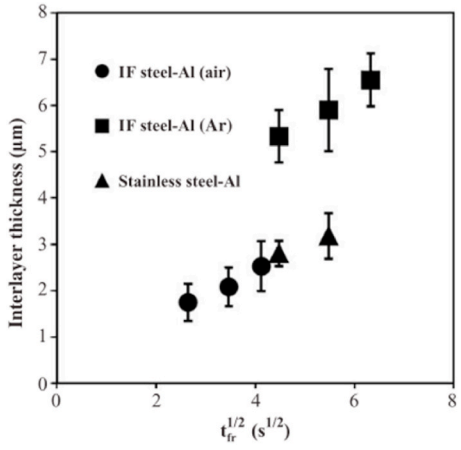

Fig. 13. Variation of the intermetallic layer thickness with friction time for Al-steel joints [62].

Cu-rich layer in the center zone, which leads to the Fe–Al layer becoming thinner in the center zone.

Another investigation showed that two types of intermetallic compound layers were formed at the friction interface of AA2219- AISI 304 IFWed: a nanoscale Fe_4Al_{13} layer and a microscale Cu-rich layer. The Fe_4Al_{13} layer had less misfit with the base material at the interface and showed less contribution to the deterioration of bonding strength, while the Cu-rich layer increased the lattice mismatch and became a weak area where cracks could initiate and propagate. Fig. 15 shows the effects of two different IMC layers on the tensile strength of the welded joints. Also, the crystal orientation of two different IMC layers with the base-metal crystal structure was investigated. Furthermore, Fig. 16 shows that during the tensile test, cracks were initiated at the interface between the ternary IMC layers and the steel or the Al_2Cu layer, which is the weakest bonding region [87].

The presence of the Cu-rich layer is a distinguishing characteristic that sets it apart from other Al alloy/steel friction welding joints. The formation of the Fe–Al layer occurs through the inter-diffusion of Fe and Al elements and metallurgical reactions at the friction interface, whereas the Cu-rich layer does not form through the diffusion mechanism of Cu elements. In addition, it is proposed that the strengthening phase precipitation-reaction-reprecipitation mechanism is responsible for the formation and growth of the Cu-rich layer [52].

Annealing experiments were used to explore the non-uniformity of IMCs at various interfacial areas in the IFW of 2A14 Al-304 SS joint to study post-weld heat treatment. As illustrated in Fig. 17, the weld strength appeared to be dropping from the center to the edge with varied annealing durations, excluding the edge location at 3 h of annealing [7]. To examine the effects of both heat and pressure on the development of IMC morphologies during thermal-mechanical coupling in the 2A14 Al-304 SS friction welded joints, Zhang et al. [16] created a thermal compression bonding approach with a self-designed device (see Fig. 18 b). According to a report, the inhomogeneous IMCs at the weld zone were caused by the wide variation of heat and plastic flow rate during the welding process. IMCs of 0.1 and 1 μm in size were visible in the joint, and none have been found at the thermal compressive weld contact.

To state clearly how preheating affects joint characteristics by using laser-assisted friction welding (LAFW), Mullo et al. [88] investigated the impact of 3-level laser power on the engineering properties and microstructural evolution of AISI 1045 Steel-2017-T4 Aluminum Alloy weld (Fig. 18a). Both the ultimate tensile strength and the thickness of the Al (Fe, Cu) interfacial layer between the linked components increased when the specimen was heated with a laser beam for 40 s in the first stage. After applying thermal laser treatment, the grain size at the steel

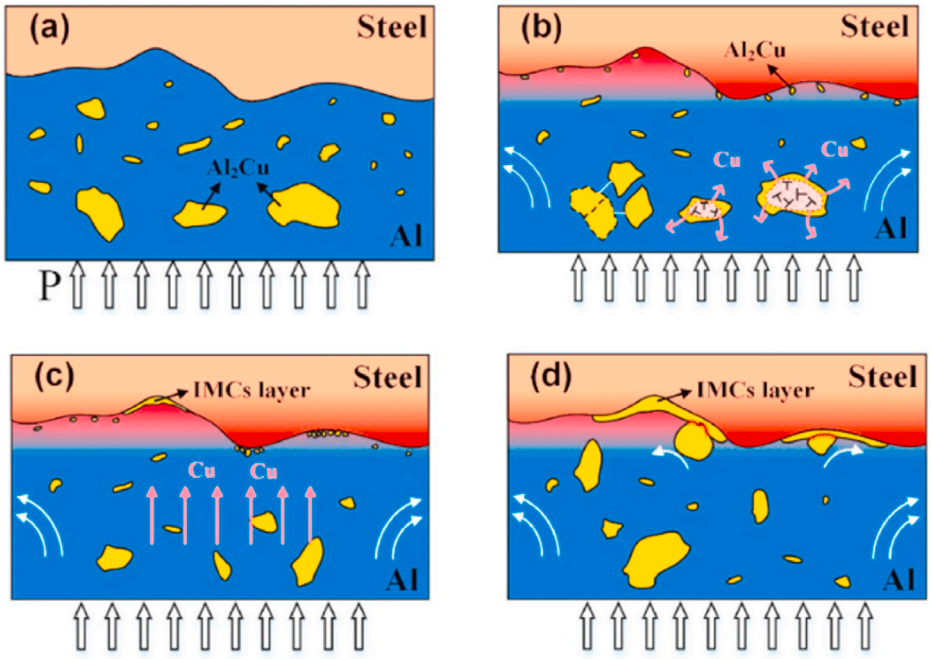

Fig. 14. Diagram of the formation mechanism of Al_2Cu at different stages: (a) initial friction stage where 2 bars are just touching by friction pressure, (b) breakage and local decomposition of Al_2Cu at high temperature, (c) accumulation of fine particles at weld interface and (d) growth of Al_2Cu particles [78].

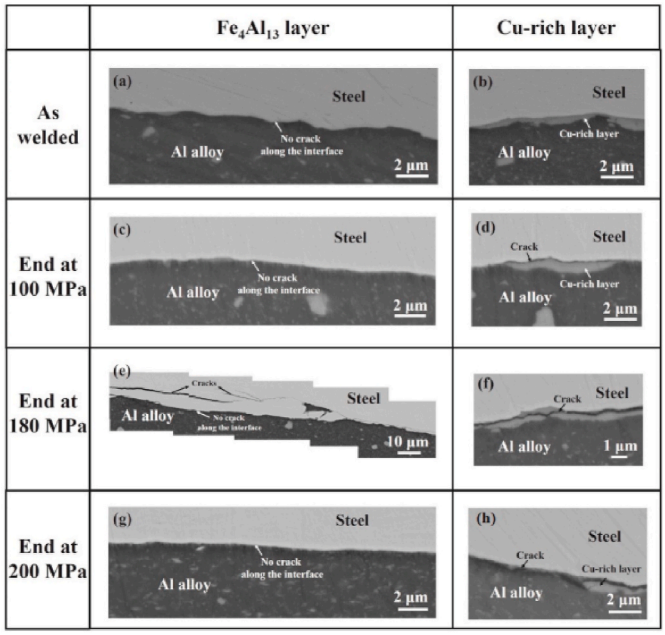

Fig. 15. Fracture behavior of Fe_4Al_{13} layer and Cu-rich layer at different tensile stages: (a) and (b) friction interface of the welded joint; (c) and (d) friction interface with tension reaching 100 MPa; (e) and (f) friction interface with tension reaching 180 MPa; (g) and (h) friction interface with tension reaching 200 MPa [87].

side has somewhat decreased in terms of microstructure evolution. The microstructure of the heat-affected zone is homogenized by the LAFW as well. A certain amount of dynamic recovery and perhaps recrystallization can be brought on in the area around the interface by the anticipated temperature rise carried on by the laser preheating. As a consequence, the average UTS value for the typical rotary friction welding technique is 119 MPa. The UTS value for the laser-assisted technique, however, is 152 MPa, which indicates an improvement of

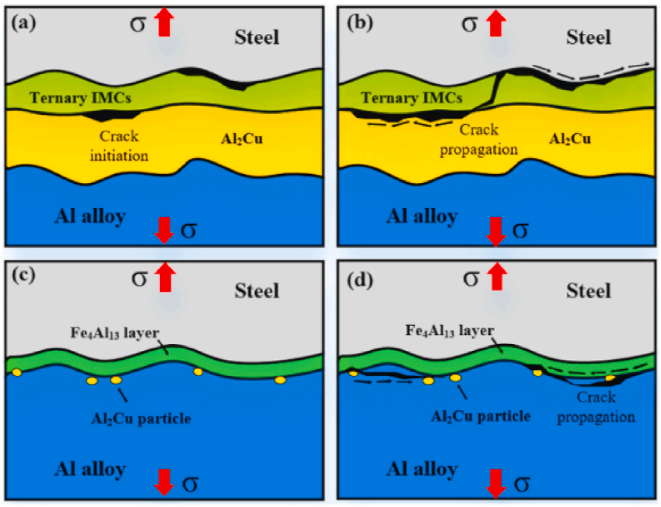

Fig. 16. Fracture behavior of the welded joint: (a) and (b) Cu-rich layer; (c) and (d) Fe_4Al_{13} layer [87].

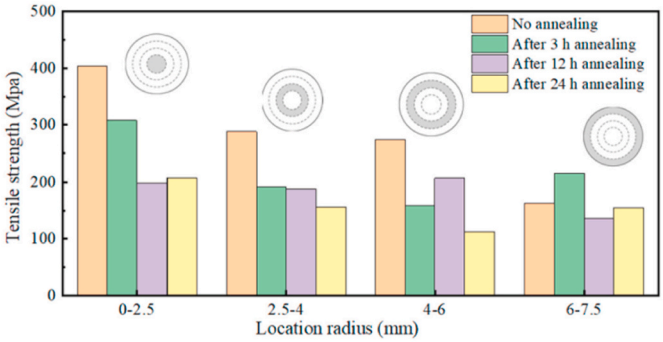

Fig. 17. Tensile strength before and after annealing at different positions of the IFW interface [7].

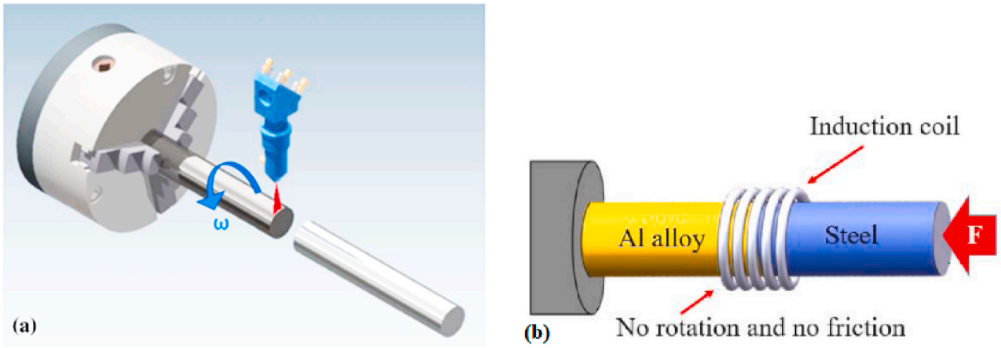

Fig. 18. Schematic of (a) laser-assisted friction welding to pre-heat [88], (b) thermal compressive device to post-heat treatment [16].

over 28%.

Several machine learning (ML) regression models, including the Gaussian process, decision tree, random forest, support vector machines, gradient boosting, and multi-layer perceptron, were trained to anticipate the ultimate tensile strength (UTS) in joints created by AISI 1045 steel and 2017-T4 aluminum alloy produced by rotary friction welding with laser aid. For the laser-assisted rotary friction welding process, the gradient boosting regression (GBR), support vector regression (SVR), and Gaussian process regression models provide the maximum precision with less than 3% error. With a coefficient of determination (R2) of more than 90.9 vs 83.2%, the GBR and SVR capacity outperform the RSM's accuracy [89].

Nickel was employed as an interlayer to an40-steel joint by Ambroziak et al. [36] The joint was created with the steps outlined: steel-nickel friction welding, heat treatment (high-temperature tempering), and one more friction welding of the accomplished steel-nickel joint with aluminum alloy has produced the most beneficial mechanical properties of the joint with tensile strength of about 270 MPa (which is approximately 70% of tensile strength for AN40 alloy). Fig. 19 depicts the joint's microstructure. There was a discernible discontinuous intermetallic dispersed phase on the AN40 alloy-nickel contact area on both surfaces (Fig. 19b).

Recently, a 3D thermal-mechanical coupling model was developed to investigate the influence of three friction coefficient models on the numerical simulation of IFW welding between 2219 Al alloy and 304 stainless steel using the ABAQUS. The first model, known as FC-TSP, considers the effects of temperature, slip rate, and pressure on the friction coefficient, with the friction coefficient decreasing as sliding velocity, temperature, and friction pressure increase. The second model, FC-TS, relates to temperature and slip rate and is obtained by setting the pressure to a constant value of the applied friction pressure. The third model, FC-T, only considers the effect of temperature. The results show that the FC-TSP model provides better accuracy in simulating IFW welding compared to the FC-TS and FC-T models. The predicted joint appearance, axial shortening distance, rotation speed attenuation, and temperature evolution are more accurate. Fig. 20 shows the experimental and simulated joint appearances of three models. However, the temperature distributions at the interface and the axial stresses are similar for all three friction coefficient models [90].

3.3. Al 5xxx series to steel joint

Using TEM, the friction weld contact between stainless steel and aluminum alloy was studied. Fig. 21 shows the amorphous layer generated at the weld contact and piled amorphous/crystalline layers. The complicated process of mechanical alloying (MA) and solid-state reaction (SSR) at high temperatures led to the formation of the amorphous phase in a solid state. It is a transitional phase before intermetallic compounds including Fe_2Al_5 are formed [91].

The interaction layer of a dissimilar weld formed by rotary friction welding 5052 aluminum alloy and 304 stainless steel including Fe_2Al_5 and Fe_4Al_{13} phases was investigated. The thickness of IMCs reached their highest value in 3R/4 rather than at the edge position, where no brittle IMCs developed. The whole joint broke at the junction and mostly showed signs of a brittle fracture [92]. Welding shifted from the outside to the interior area, as seen in Fig. 8 [6]. Also, it was noted that at the AA 5052-A 36 steel contact, the IMC layer was larger on the periphery than in the center. FeAl and MgO were most likely the constituents of this layer [93].

The impact of PWHT in the AA 5052 –SS 304 joint was examined in a separate investigation. The thickness of the IMC layer remained constant during post-weld heat treatment at 250 °C for 20 min, while the UTS of the whole joint rose from 153 MPa to 161.4 MPa. Also, the UTS difference in the radius direction was reduced, which was advantageous for the engineering application. The ultimate tensile characteristics of the whole joint deteriorated when the annealing temperature was over 350 °C, although the thickness of the IMC layer increased by increasing annealing time. After PWHT at 450 °C, the grain size increased with longer annealing times. Boundaries and dislocations were also reduced, and storage energy was discharged. The IMCs' circumstances for

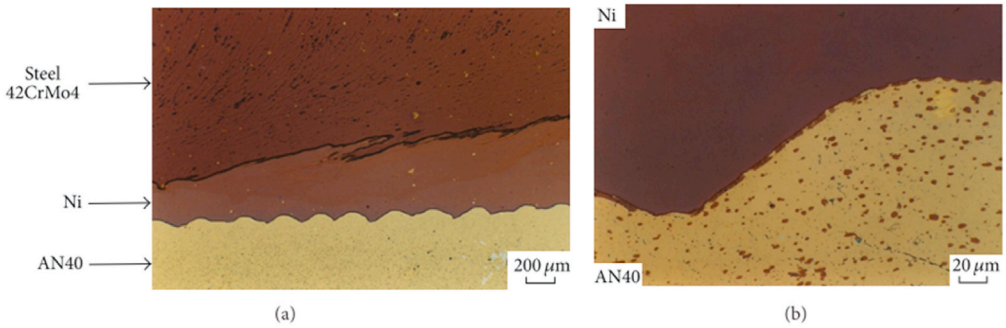

Fig. 19. (a) The microstructure of the 42CRMo4 steel-AN40 alloy joint with the nickel interlayer and (b) a fragment of an enlarged microstructure of the nickel-AN 40 alloy bounding zone [36].

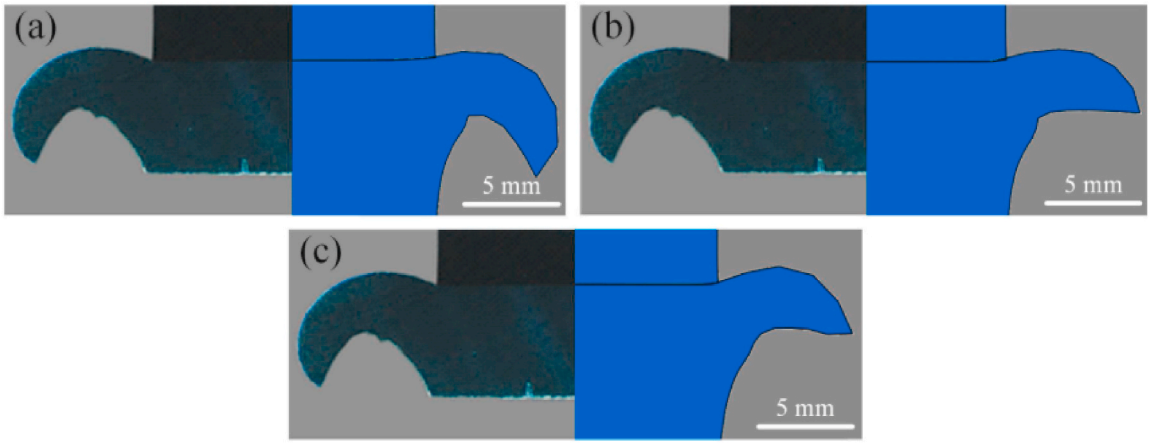

Fig. 20. Joint appearances verification of (a) FC-TSP model, (b) FC-TS model, and (c) FC-T model [90].

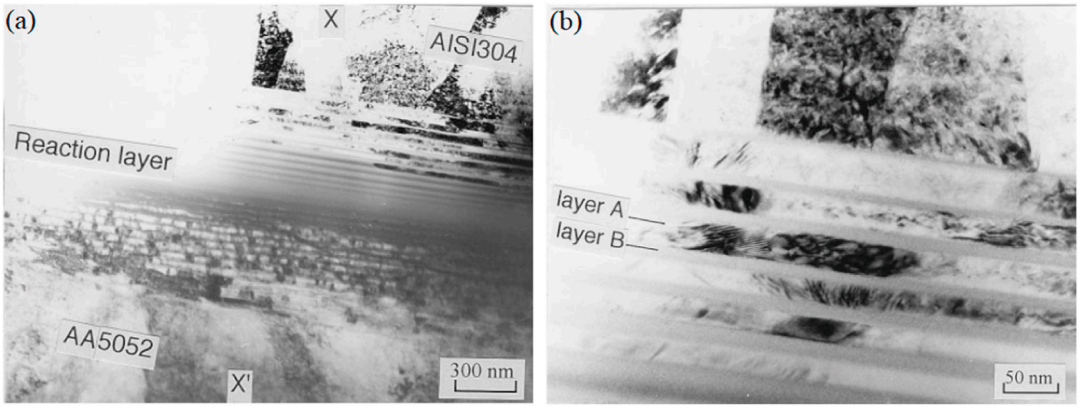

Fig. 21. TEM image of (a) friction weld interface (b) stacked layers between stainless steel and reaction layer [91].

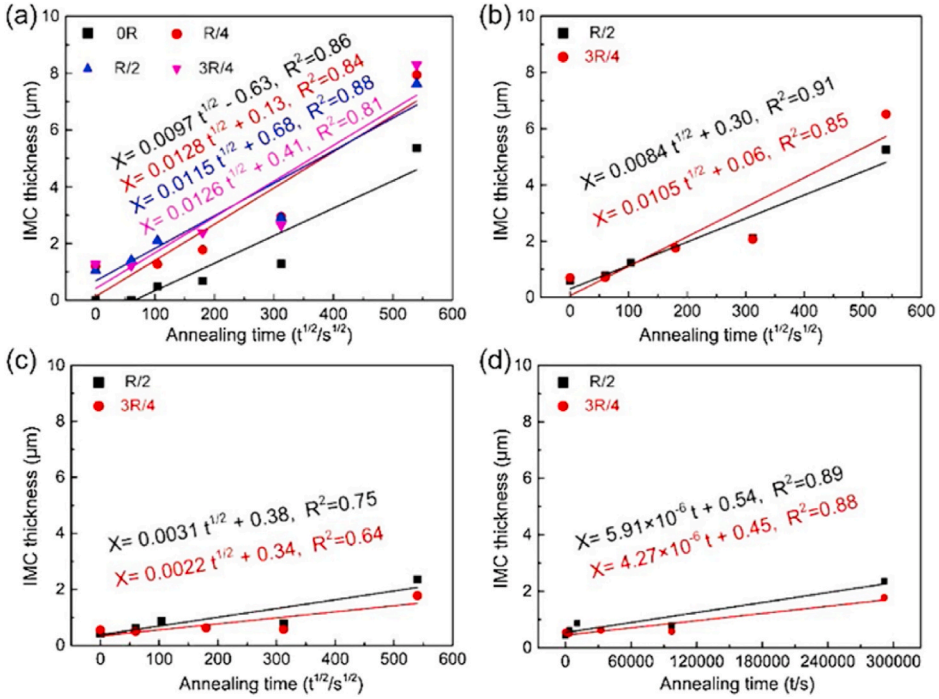

Fig. 22. Relationship between the thickness of IMC layer X and the square root of annealing time at 450 °C: (a) IMC layer, (b) Fe_2Al_5 phase, (c) Fe_4Al_{13} phase, and (f) variation of Fe_4Al_{13} phase thickness X with annealing time at 450 °C [10].

nucleation and growth changed when the diffusion mode switched from short-circuit diffusion to bulk diffusion. The IMC layer's development varied from the parabolic rule. The growth of the Fe_2Al_5 layer, as seen in Fig. 22, was determined to follow the parabolic law, whereas the growth of the Fe_4Al_{13} ($FeAl_3$) phase was linear [10].

By contrasting the results seen in the A5052/S45C weld with the results seen in the A5052/S10C weld, the effects of the C percentage of the steel on the development of the IMC layer and UTS of the friction-welded intersection of Al alloy to steel have been explored. The summary of the findings shows that a very fine grain region was found in the steel near the intermetallic compound layer, indicating that the steel surface had experienced significant plastic deformation during the friction step. Furthermore, in direct relation to the amount of friction, the fine grain region's thickness had risen. The thickness of the IMC layer rose similarly compared to the fine grain region, following a trend that was essentially irrespective of the C percentage of the steel and the composition of the Al alloy (Fig. 23a). Furthermore, the A5052/S45C joint's IMC layer expanded at a slow rate than the A5052/S10C joint, yet both joints' IMC layer thickness rose almost proportionally to friction time (Fig. 23b) [94].

The mechanical and metallurgical characteristics of friction-welded joints between A36 steel and AA 5052 aluminum alloy using different welding parameters revealed that although the microstructure of the A36 steel remained relatively unchanged from the base metal, the microstructure of the AA 5052 at the weld interface varied significantly (Fig. 24). The 5052 alloy's microstructural characteristics can be divided into four regions, which are comparable to those seen in friction stir welding: (a) the DRX region, which has refined and equiaxed grains with a size ten times smaller than the base metal due to strong plastic deformation and heat generation during the friction welding process; (b) the heat and deformation affected zone (HDZ), which exhibits a 'flowing' grain structure from the central to the peripheral part, leading to elongated grains; (c) the heat affected zone (HAZ), which is located outside the HDZ and can only be identified by hardness tests; and (d) the base metal. The deformed region expanded with increasing friction time and contracted with increasing upset pressure [93].

It was determined to join $AlMg_3$ alloy with X10CrNiTi189 steel and use three types of interlayers (CP Al), (Ti and CP-Al), and (Ti and $ALMg_3$). By using pure aluminum to create joints, the tensile strength is equivalent to 185 MPa, and the rupture occurs at the aluminum-steel contact boundary. When used as a second layer, the $AlMg_3$ alloy has enabled the fabrication of welds with a 346 MPa strength (the fracture at the $AlMg_3$-steel boundary) and the achievement of bending angles more than 120° in mechanical bending tests. This behavior could be the result of the low thickness of the entire extra interlayer allowing stress transfer to occur in the joint under bending, regardless of the intermetallic phases developing on the bonded $AlMg_3$ alloy-X10CrNiTi189 steel. On the $AlMg_3$ side, the deformation was seen somewhere under the titanium layer. Consequently, it was possible to create a joint with high strength and a reasonably high bending angle in the $AlMg_3$ alloy-X10CrNiTi189 austenitic steel joints by employing the titanium and $AlMg_3$ interlayer [36].

3.4. Al 6xxx series to steel joint

The friction-welded joint between AA 6063 and SS 304 thin-walled pipes was studied for the effects of friction time, forging stress, and interfacial bonding. The results indicated that though the bond with a friction time of 1.6 s had the IMC interlayer at the weld contact, the bond with a friction time of 0.4 s did not. Compared to the joint without flash, the joint with flash had a greater joint performance. The worn-out inner flash of A6063 was the cause of this outcome. Because A6063's inner flash was adhered to the inside of the SUS304 pipe, the precise joint performance should be assessed by the joint lacking flash [95]. Additionally, the joint must be made using a high upset pressure, such as 240 MPa, and with the appropriate friction time (1.5 s), when the temperature on the weld zone reaches approximately 623 K or higher, to achieve 100% joint performance of AA 6063-SS 304 bars, rupture in the A6063 base metal with no defect at the weldment, and bend ductility of 90°. The AA 6063 side of the weld, however, showed a minor softened region close to the weld boundary. So, it is preferable to eliminate as much of the softened region from the joint as feasible. While it may be assumed that a water-cooling operation will be successful in removing a softened area from a joint, tensile strength, the fractured point, and the distribution of weld hardness were not different among an air-cooling process and an iced water-cooling process [20].

The microstructure and mechanical properties of the AA 6061-T6/304 stainless steel joints welded by inertia friction welding (IFW) and continuous drive friction welding (CDFW) were investigated and compared. The microstructure of the fully dynamic recrystallized zone (FDRZ) had grain sizes below 0.1 μm in both joints. The IFWed joint had an average FDRZ width of about 5 μm, while the CDFWed joint had an average FDRZ width of about 2 μm, indicating that CDFW resulted in a finer grain size. The IFWed joint exhibited higher hardness and maximum tensile strength compared to the CDFWed joint, which could be attributed to the thickness of IMC at the welding interface [96].

Gotawala et al. [97] investigated the influence of IMC thickness and microstructure variations at the interface of AA6061 and mild steel joints through displacement control mode on a CNC milling machine. They conducted experiments at three feed rates of 10, 20, and 30 mm/min, and two rotational speeds. The results showed that lower rotational speeds and increased friction time lead to grain refinement due to strain accumulation and CDRX, while higher rotational speeds and temperatures promote grain growth with increased friction time.

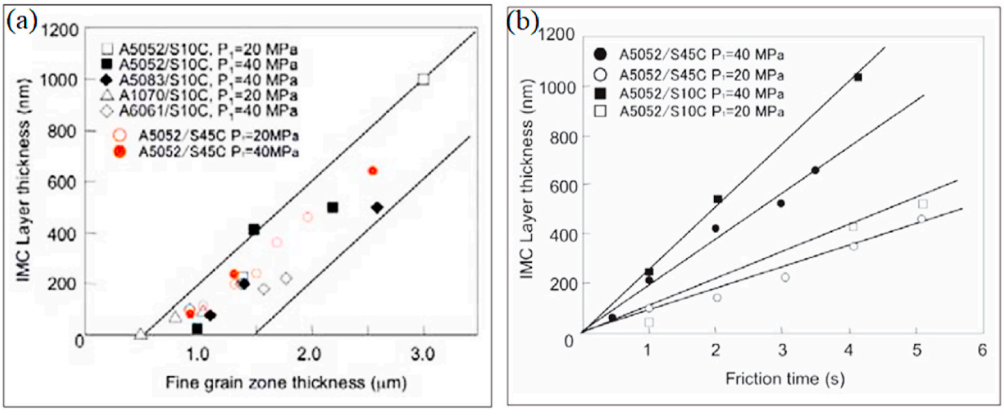

Fig. 23. Thickness of IMC layer (a) vs. thickness of the fine grain zone in steel substrate next to the IMC layers observed in joints of various Al alloys to steel S10C and steel S45C (b) vs. friction time [94].

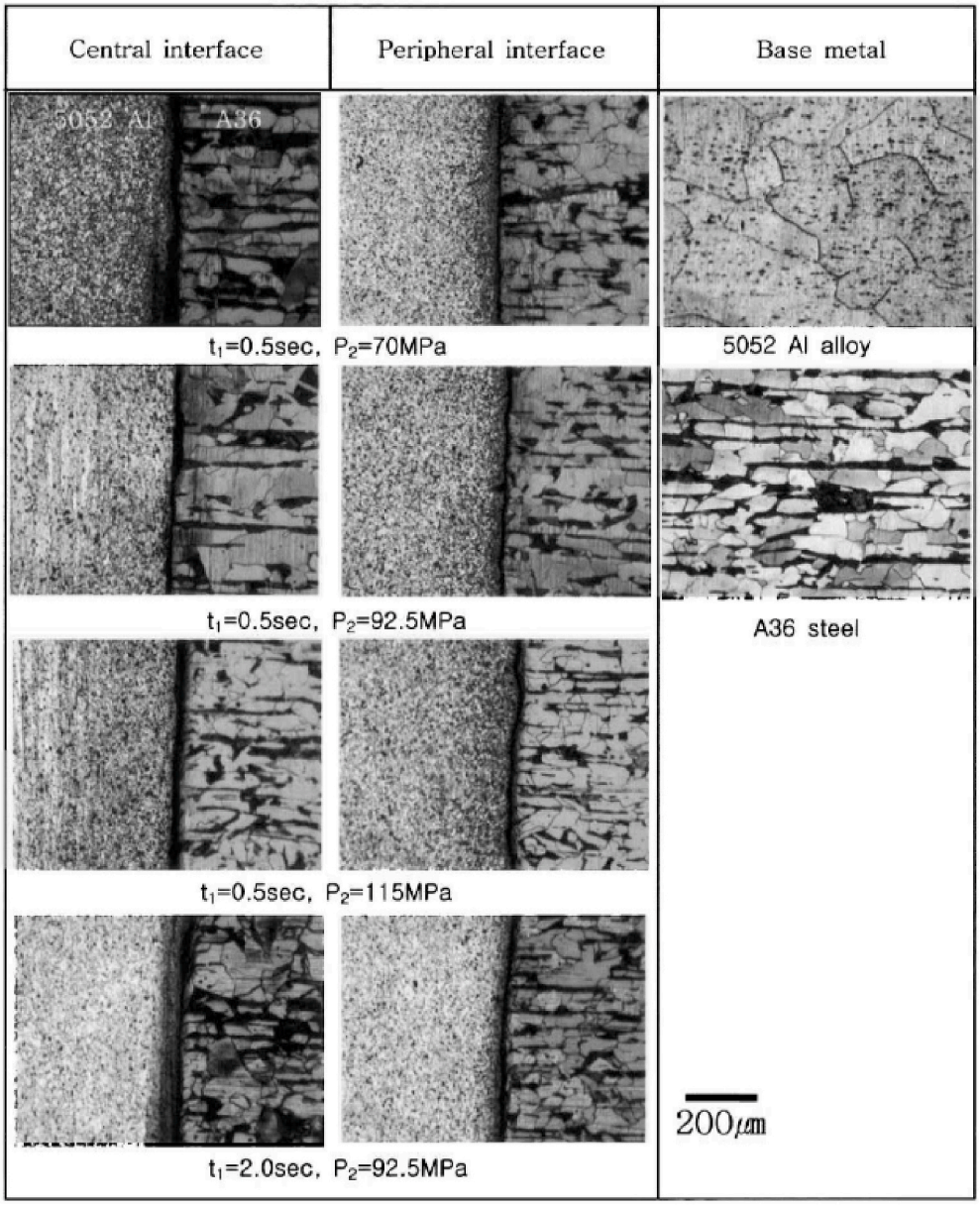

Fig. 24. Microstructures of the base metals and weld interfaces at central and peripheral regions for different welding parameters [93].

The reduction in IMC thickness and increase in DRX region thickness along the radial direction from periphery to center hinder crack growth. In the IMC-rich regions near the periphery, brittle failure is observed, while ductile failure is noticed near the center. Ultimately, the combination of IMC and DRX region thickness resulted in the maximum tensile strength for the joints fabricated at the intermediate feed rate of 20

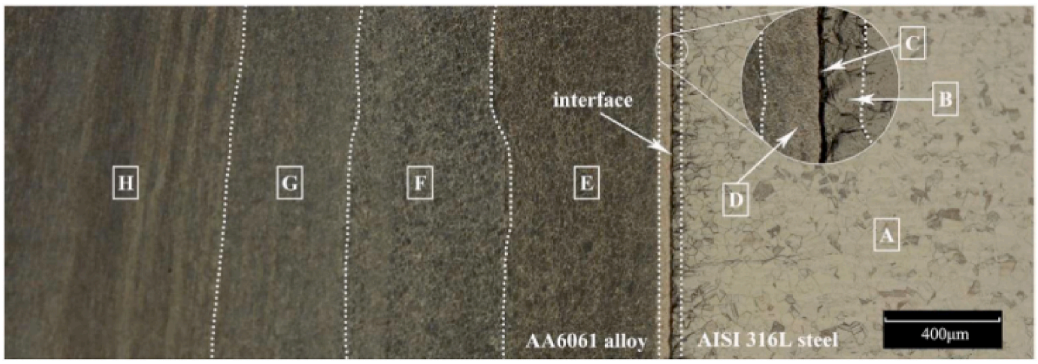

Fig. 25. The division of the joint for partitioning elevation when friction time was 40 s [18].

mm/min.

Wan et al. [18] conducted a study to investigate the joining of AA6061 and AISI 316L steel with and without grooves. This research identified eight distinct zones, with the presence of certain zones dependent on friction time (as depicted in Fig. 25). Region A on the AISI 316L side refers to the base metal (BM), whereas region B corresponds to the heat- and deformation-affected zone (HDZ). In the HDZ, crystal grains were notably smaller, and the crystal boundaries were expanded due to the accumulation of dislocations, as demonstrated in Fig. 26b.

The microstructure of AA6061 alloy can be classified into several distinct regions, including region C or the interfacial zone (IZ), which is characterized by the presence of intermetallic compounds. Region D, the solid solution zone, appears light in color in Fig. 26b, indicating insufficient precipitation of secondary phases. This is because region D experienced the highest temperature and fastest cooling rate, allowing insufficient time for secondary phases to precipitate into the matrix. Region E, or the partial secondary recrystallization zone, is characterized by refined and equiaxed grains resulting from recrystallization, with a few large-sized grains observed in Fig. 26c. The nucleation and growth of new grains occur under the coupling effect of plastic deformation and high temperature, although the heat input and time are insufficient for further growth, and only a few grains annex smaller grains to grow, as indicated in Fig. 26c. Region F, or the recrystallization zone, consists of equiaxed grains that emerge when the temperature is adequate for recovery, and they grow rapidly, as shown in Fig. 26d. Region G, or the partial recrystallization zone, is challenging to identify entirely as it contains only some equiaxed grains. This is because the temperature in this region is lower than that in the recrystallization zone. Finally, region H, or the plastic deformation zone, is situated far from the interface and less affected by friction heat, and the heat input is insufficient for recrystallization to occur [18].

Reduction of IMC layer thickness was observed with decreasing friction time from 40 to 10 s, with the thickness decreasing from 4 to 0.2 μm. Additionally, machining a 15° welding groove on the end of the steel facilitated the thinning of the IMC layer to a thickness of 0.3 μm [18].

The effect of friction time (T2) on the microstructure of four specimens (T2 = 4, 10, 25, and 40 s, respectively) is depicted in Fig. 27a–d. At a relatively short T2 of 4 s, only a plastic deformation zone (region H) is visible on the aluminum side due to insufficient heat (Fig. 27a). Increasing T2 to 10 s results in the formation of a lighter-colored solid solution zone (region D) between the joint interface and the plastic deformation zone (Fig. 27b). This suggests the dissolution of secondary phases near the interface due to elevated temperature. However high heat conductivity coefficient of aluminum and the rapid cooling rate during upsetting stage prevents further precipitation, maintaining the solid solution state. When T2 is increased further to 25 s, the width of the solid solution zone (region D) significantly expands (Fig. 27c). This finding revealed that as the friction time increased, more heat was transferred to the aluminum alloy side, allowing secondary phases to dissolve into the aluminum matrix from a wider range. Additionally, a partial recrystallization zone (region G) appears due to sufficient temperature for partial recrystallization during upsetting stage. However, the process remains incomplete due to a drop in temperature below the recrystallization threshold. The microstructure of the joint at T2 of 40 s exhibits a complete recrystallization zone (region F) near the interface and a partial secondary recrystallization zone (region E). This suggests sufficient heat for complete recrystallization followed by secondary recrystallization at higher-temperature regions (Fig. 27d). Fig. 27e illustrates the impact of a welding groove on the overall microstructure, which remains similar to the specimen with 25 s but with variations in the width of the solid solution zone. This result revealed that the welding groove facilitated the expulsion of plasticized aluminum alloy. Meanwhile, some zigzags appeared on the edge of the solid solution zone, which coincided with this point [18].

Presently, there exist two approaches to regulate the effect of Fe_xAl_y in welding, which include either eliminating the IMCs or generating a thin and uniform layer of these phases. According to Vyas et al. [26], the Fe_3Al intermetallic compound was identified as the product of the reaction between Al–Fe elements from the reaction layer, which was continuous with a varying thickness between 1.1 μm and 2.0 μm at pipe joints made of AA6063-T6 and SS 304L materials. In contrast, Hincapié et al. [98] observed the absence of IMC in the friction welding of AA 1100-SS 304 and AA 6061-SS 304 due to the low heat input generated during the process, which was below the threshold value of 545 °C. The formation of IMC requires extended periods to facilitate atomic exchange and the reaction and formation of the compound, as demonstrated by Nicholas & Crispin's experiment on aluminum and steel joints using diffusion welding at 50 MPa for 30 min (Fig. 28). Equation (1) determines the IMC thickness based on the temperature, indicating that an IMC layer with a thickness of 15 μm is achievable within the experimentally measured temperature range of 243 and 521 °C, provided the

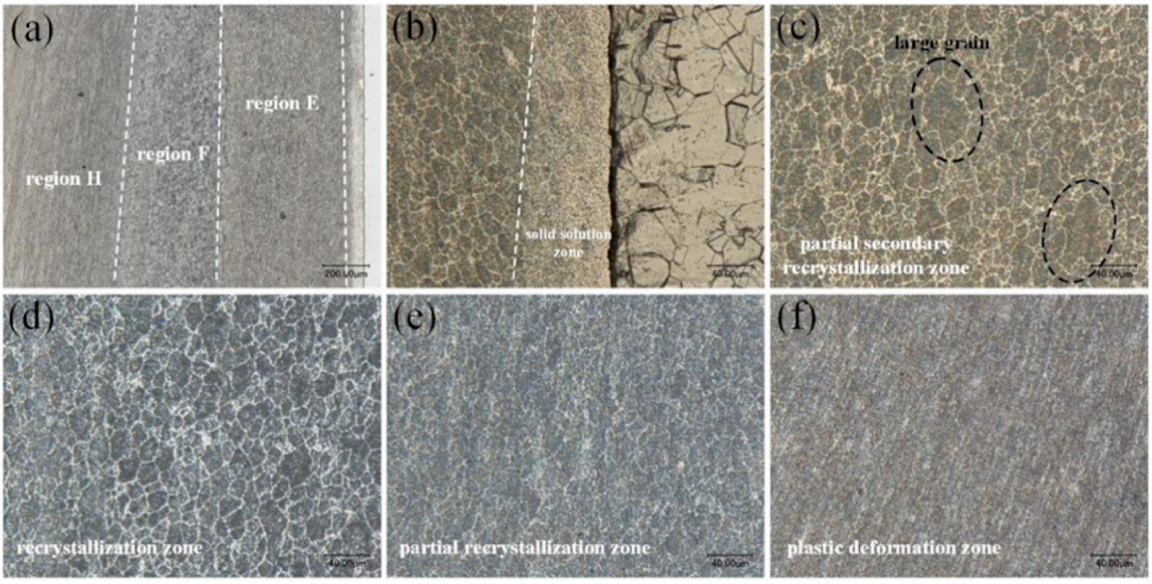

Fig. 26. Microstructure characteristic of typical region shown in Fig.24 (a) Region (D–H) (b) region D, the solid solution zone (c) Region E, the partial secondary recrystallization zone (d) Region F, the recrystallization zone. (e) region G, the partial recrystallization zone (f) Region H, the plastic deformation zone [18].

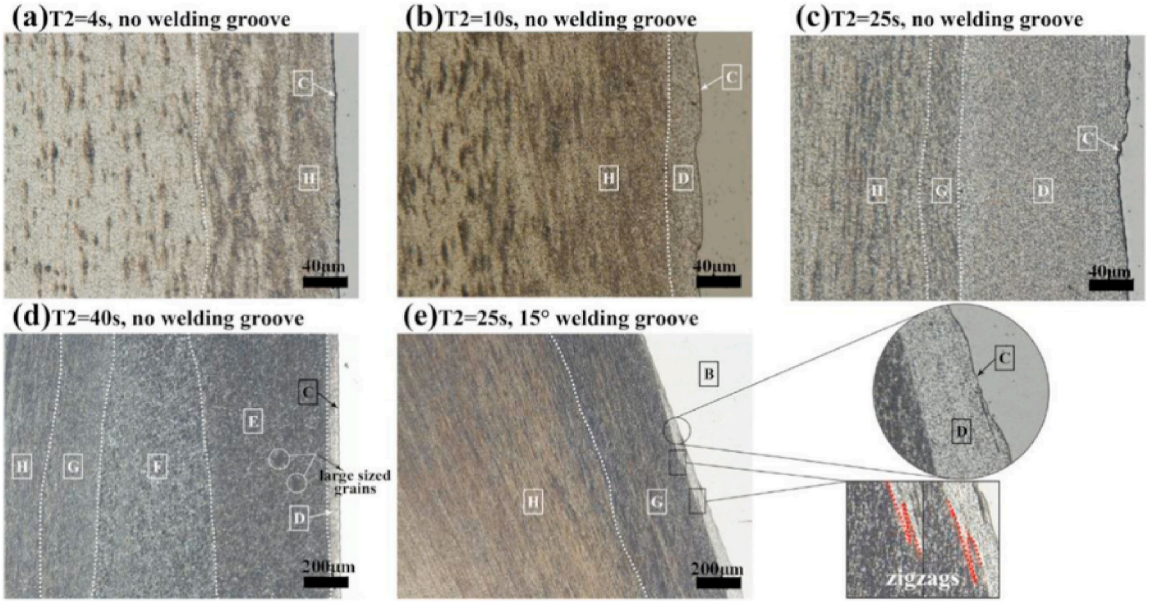

Fig. 27. The effects of friction time and welding groove on the microstructure of the joints [18].

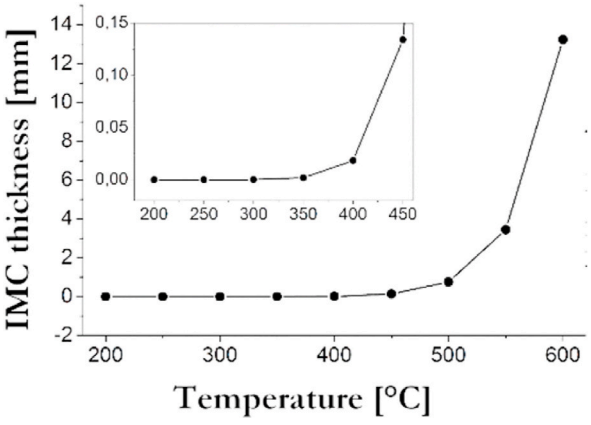

Fig. 28. Thickness and temperature relationship for IMC formation for aluminum-steel joints using the diffusion welding process [98].

processing time is 30 min. However, this duration is impractical in the CDFW process to promote the formation of IMCs.

Ma et al. [32] carried out research on the interfacial layer transformation in the inertia friction-welded joint of AA6061 and 304 stainless steel. They used high-resolution transmission electron microscopy (HRTEM) to investigate the transformation from the amorphous phase to the mixed phase and eventually to a fully crystallized Fe_2Al_5 intermetallic compound. The plastic deformation/flow/heat input caused the deconstruction of the crystallized reaction layer, which resulted in an expanded window for the amorphous phase. The temperature directly affected the final interfacial microstructure type and thickness. According to the mechanical property measurements, the joint's bonding strength was high when the nanosized amorphous and mixed phases were present. However, increasing the IMC layer thickness to more than 100 nm caused interfacial failure with low bonding strength, which may be attributed to different residual stress distributions in joints produced by various welding techniques. Fig. 29 illustrates the local bonding strength of the joint with the thickness of the reaction layer. It was observed that the joint strength was closely associated with the type and thickness of the reaction layer.

Fig. 30a shows that the Al alloy didn't undergo severe plastic

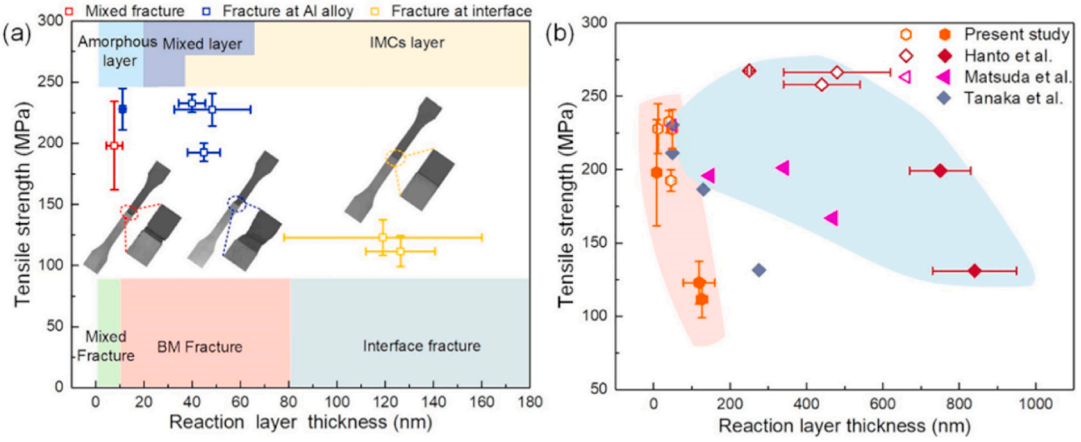

Fig. 29. (a) Relation between the reaction layer thickness with different crystallinities and joint strength and (b) comparison of the relationship between the reaction layer thickness and Al alloy/steel joint strength in different studies. The open symbol in indicates the fracture occurred on the Al alloy side, while the closed square represents the interfacial failure [32].

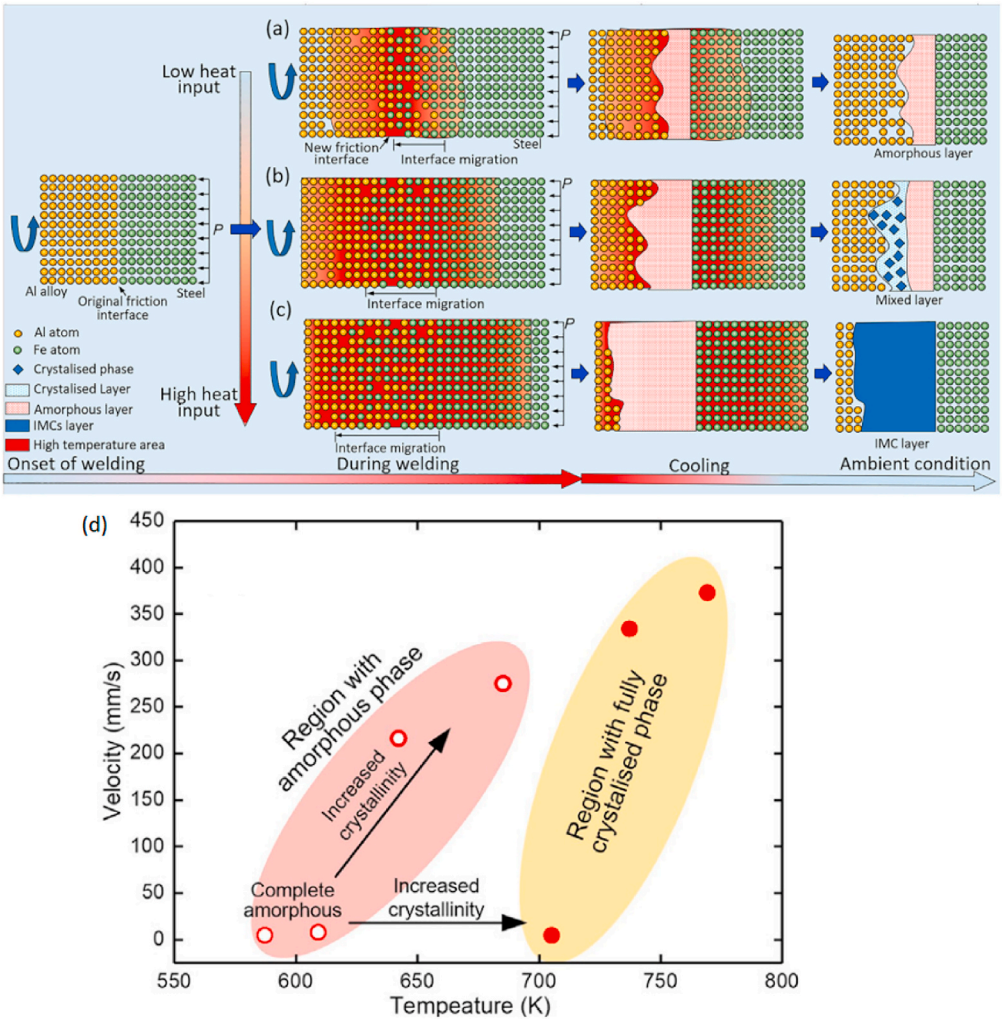

Fig. 30. Illustration of the possible reaction process during IFW: (a) formation of the complete amorphous phase, (b) formation of mixed-phase, (c) formation of IMC, and (d) The relation of the phase type as a function of velocity and peak temperature [32].

deformation during the oxidation extrusion, resulting in limited interface migration. The low processing temperature in the cooling stage may have prevented the Fe–Al amorphous phase from transforming into the crystallized phase (Fig. 30a) [32]. Fig. 30d illustrates the relation between phase type and velocity/peak temperature. Heat input had a significant impact on joint mechanical properties. A low heat input resulted in an un-welded zone, while a higher heat input produced sub-micron-sized intermetallic compounds. Rotational speed and higher heat input allowed for the formation of a nanoscale mixed layer containing partially crystallized and amorphous layers. The formation of IMCs could be from the transformation of the amorphous phase or the direct reaction between Fe and Al. The initial microstructure could be preserved with the right temperature, but a thicker IMC layer could negatively affect corrosion resistance (Fig. 30b) [99]. When heat input and rotational speed were further increased, it was likely that the formation of IMCs could be from either the transformation of the amorphous phase or the direct reaction between Fe and Al. As illustrated in Fig. 30c, heat input at a sufficient driving force may preserve the initial microstructure and promote phase transformation [32]. However, a thicker IMC layer might negatively affect the joint's corrosion resistance [78].

Heppner et al. [100] recently introduced a suitable finite element modeling to estimate the bonding strength for friction welding of structural steel S355 to AA6061. This approach uses the bond formation (R) during the welding process to calculate the bonding strength (β), which is subsequently represented by the mean of a correlation function. A variety of welding experiments were carried out with varying process parameters to develop the correlation function, and the bonding strength was then examined. The bonding strength indicator in this approach depends on temperature (T) and strain rate ($\dot{\varepsilon}$), both of which are easily influenced by welding parameters like friction pressure and friction time. The distribution of the measured bonding strengths, the computed average indicators, and the identified functional relationship are shown in Fig. 31.

The influence of surface roughness on the properties of joints was investigated by Ashfaq et al. [101], who found that treatments such as face milling or mechanical polishing did not have a significant effect on the properties of the CDFWed AA6061/stainless steel joint. In contrast, increased surface roughness led to an increase in tensile strength for the IFWed AA6061/carbon steel joint [102]. Further study of the effect of surface roughness was conducted by Ma et al. [102], who prepared IFWed joints between AA6061 alloy and 304 stainless steel surfaces with varying degrees of roughness, including as-machined, 80 grit, 240 grit, and polished surfaces (Fig. 32). The as-machined joint showed a sizable un-bonded area in the central region due to limited material flow and a relatively low processing temperature, as well as both a reaction layer and defects in the outer region.

In the Al alloy/polished steel joint, an amorphous layer formed in the central interfacial region, leading to an intimate contact. Conversely, the Al alloy/ground steel joint showed signs of an un-bonded defect in the

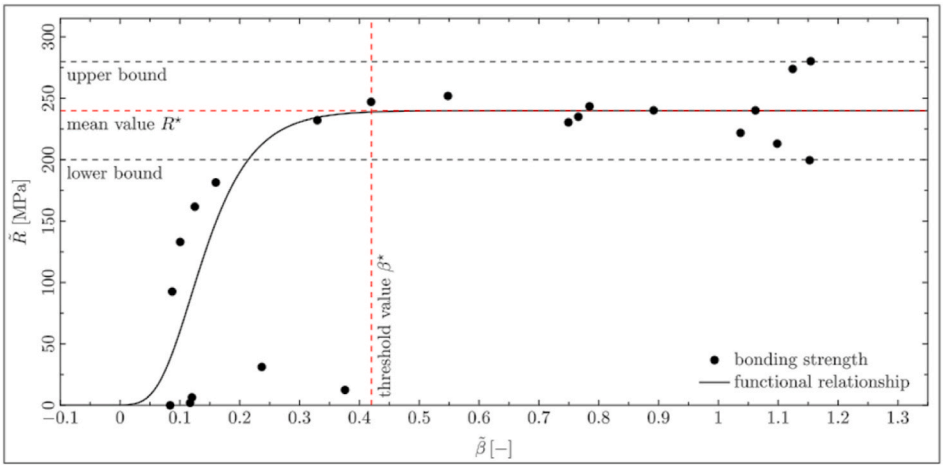

Fig. 31. Determined functional relationship [100].

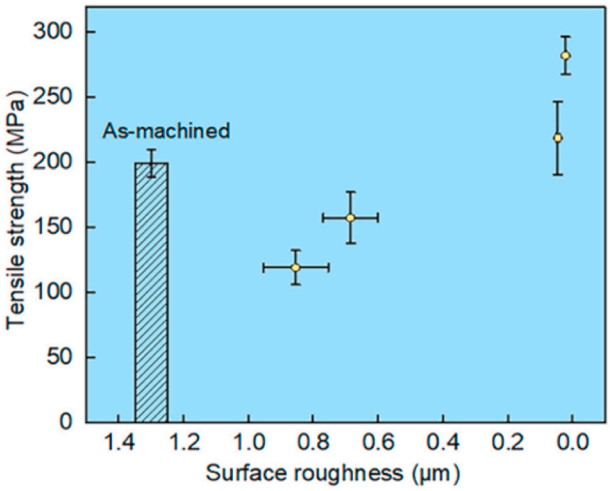

Fig. 32. Tensile strength of the friction welded joint of Al alloy to steel with different surface roughness [102].

central area, with the outer region displaying a reaction layer that included a partially crystallized Fe_2Al_5 layer and an amorphous layer. An interface of two distinct layers was observed in the 1/2R region of the Al alloy/polished steel sample, as seen in Fig. 33: layer I, which was partially crystallized and in contact with the Al alloy, and layer II, an amorphous layer next to the steel surface. Upon reducing the surface roughness, an increase in joint strength was noted, as shown in Fig. 34. The Al alloy/ground steel joint exhibited a lower degree of local ductile fracture than the Al alloy/polished steel, likely due to the presence of grinding trenches and an un-bonded area, which reduced interface bonding strength. As surface roughness decreased, the fracture surface became rougher, as expected from the tensile property measurements of the joint [102].

In another study, Ma et al. focused on preheat treatment on properties of AA 6061 to as-machined or polished AISI 304 stainless steel joints made by IFW. The main conclusions were drawn as follows [25].

1. The interfacial reaction layer in the 1/2R region of an Al alloy to steel joint consisted of a partially crystallized Fe_2Al_5 layer (layer I) and an amorphous layer (layer II), as observed in Fig. 35. Despite the Gibbs free energy difference between the formation of IMCs and the amorphous phase, increased shear effect during the reaction may have led to the formation of the amorphous layer. However, the amorphous layer was found to be unstable, and preheat treatment could promote the growth of layer I and suppress the amorphous layer, resulting in a slightly thicker layer I and a discontinuous reaction layer in the peripheral region.
2. Preheat treatment was also found to reduce the un-bonded or weakly bonded areas in the central region, although a larger peripheral region with low bonding strength limited further improvement in joint strength.

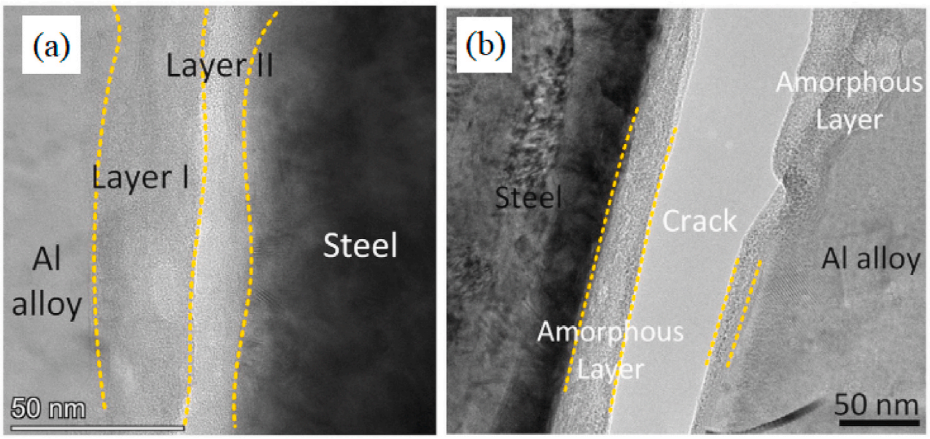

Fig. 33. HRTEM. Image of the interfacial microstructure of IFWed Al alloy to polished steel: (a) ½ R region, (b) central region [102].

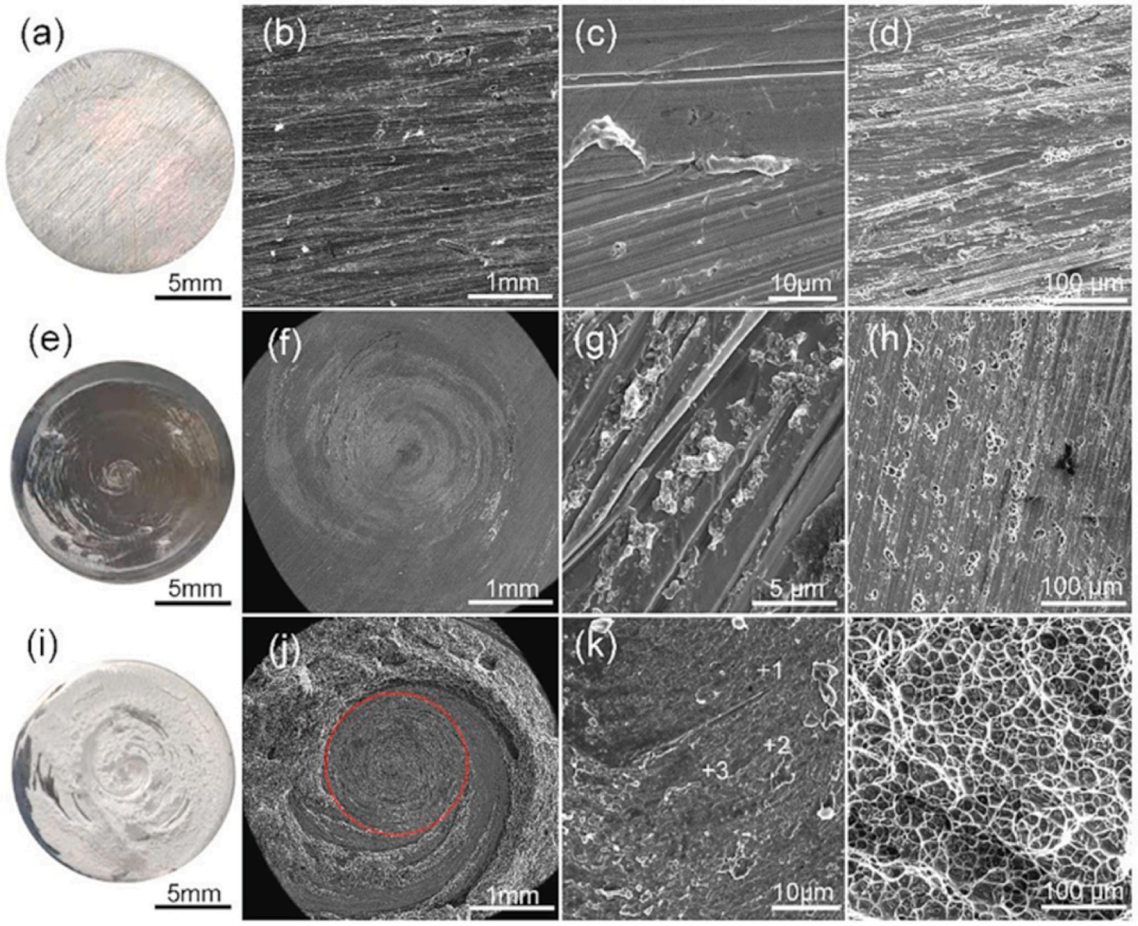

Fig. 34. Fractography of IFWed joint of Al alloy to steel ground by different grit sandpapers ((a)–(d) 80 grit, (e)–(h) 240 grit and (i)–(l) polished) at different characteristic region: (a), (e) and (i) macroscopic fracture image on steel side, (b), (f) and (j) central region, (c),(g) and (k) magnified central region and (d),(h) and (l) 1/2R region [102].

3. After preheating treatment, the Al alloy/as-machined joint showed an increased tensile strength with the highest strength of 270 MPa, a 10% improvement over the as-welded joint. Conversely, the Al alloy/polished joint exhibited a slightly decreased tensile strength following preheat treatment, from 282 MPa to 267 MPa, attributed to the larger peripheral region and smaller 1/2R region with high bonding strength. These findings suggest that preheat treatment can improve interfacial bonding strength and thereby enhance joint properties, depending on the joint's initial state and the degree of peripheral region involvement.

Kimura et al. [103] outlined the distinguishing properties of the joint created by friction welding between Al–Mg–Si alloy (A6063) and austenitic stainless steel (304SS) that underwent post-weld heat treatment (PWHT) at different forge pressures of either 30 or 240 MPa. The initial welded joints had no occurrence of an IMC interlayer at the point of welding. Adding magnesium in the Al alloy causes the IMC interlayer to form, with joint strength exhibiting a less pronounced tendency as magnesium content increases. Meanwhile, silicon in the Al alloy is limited in generating the IMC interlayer due to its inability to diffuse into both Al and Fe. It was hence inferred that the generation of the IMC interlayer at the weld interface of the A6063/304SS joint via the PWHT process was directly influenced by the magnesium and silicon content.

The condition of PWHT can be characterized by the Larson-Miller parameter (LMP), which can be expressed by the equation shown below. The A6063/304SS joint would fracture at the weld interface through the PWHT process when the LMP exceeded approximately 16,000, due to the creation of the IMC interlayer. When LMP crossed the threshold value, the joint efficacy experienced a significant decline (Fig. 36). This parameter can estimate a construction's lifetime and explain the cause of the joint fracture through the PWHT process. LMP was defined as shown in the following equation [103]:

$$LMP = T(log_{10}\, t + 20) \tag{3}$$

Where T is heating temperature (K), and t is holding time (h).

Herbst et al. [60] have examined how heat treatment affects the development of IMCs in their research. Different T6 heat treatments were applied to friction-welded rods consisting of the metal alloys AW6082 aluminum and 20MnCr5 (i.e., solution annealing and aging). Tensile tests and the thickness of the IMC layer along the bond zone were used to calculate the strength properties of the joints. The solution annealing temperature and time have a significant impact on the bond strength. The bond strength is significantly decreased when solution annealing conditions (540 °C, lengthy dwell durations) are used to achieve the high-strength T6-state in the aluminum component. A higher bond strength was achieved compared to the as-welded state at a lower solution annealing temperature of 500 °C (Fig. 37c). With rising mean IMC-layer thickness, the weld strength demonstrated a linear decline. The mean bond strength (UTS), evaluated in the current investigation, is shown as a function of the average IMC layer thickness (d) in Fig. 37a. The linear pattern from the research (Fig. 37b) could be validated.

An alternate method for enhancing friction welding effectiveness is by modifying faying surfaces or changing shape designs, as discussed earlier. Six different experimental methods were performed on weld

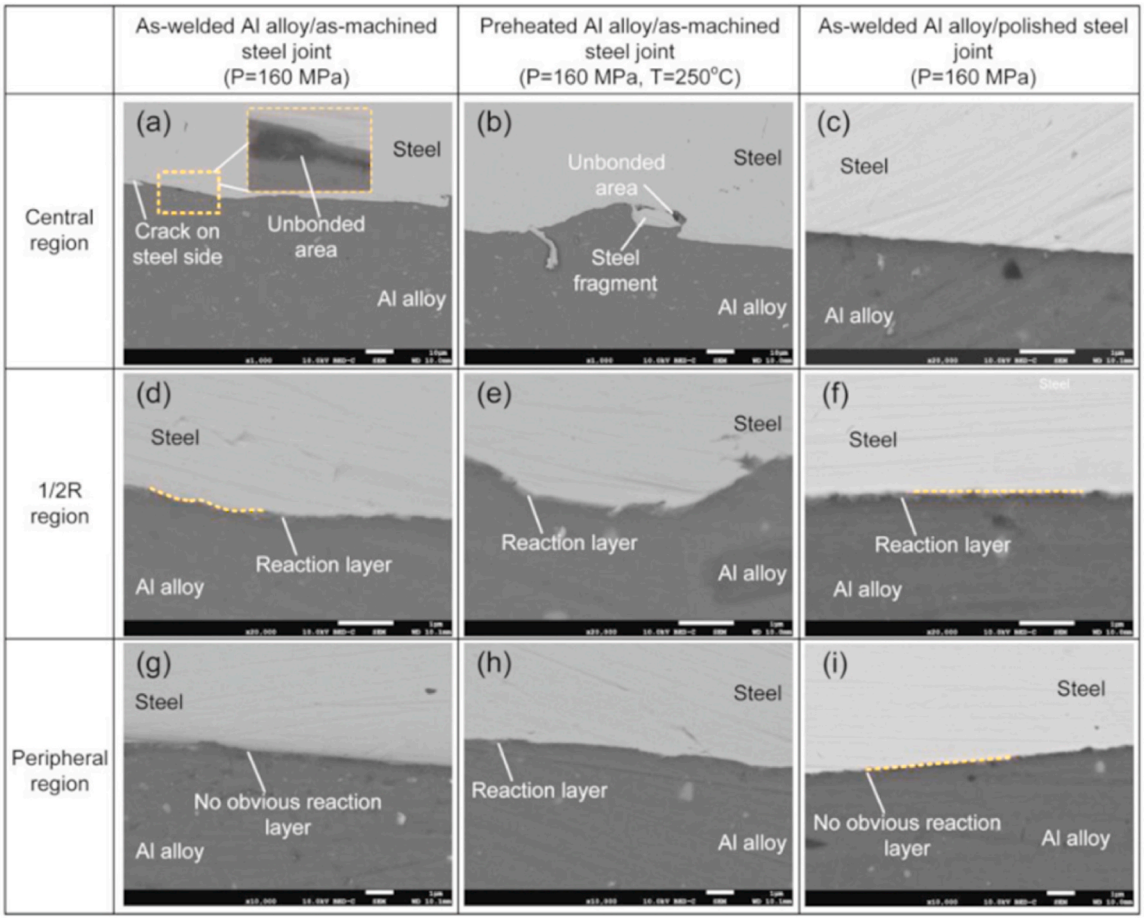

Fig. 35. Interfacial microstructure of the Al alloy/as-machined steel and Al alloy/as-polished steel joint welded at a friction pressure of 160 MPa with/without preheat treatment of 250 °C [25].

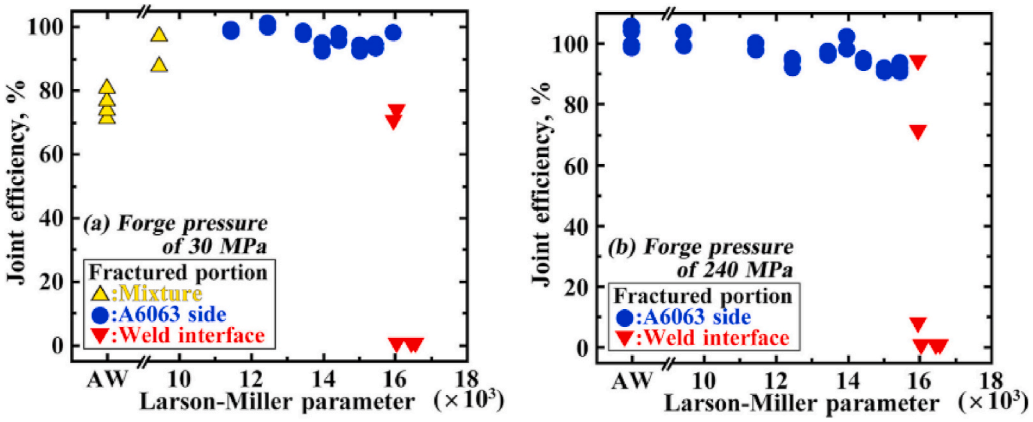

Fig. 36. Relationship between joint efficiency and Larson-Miller parameter for A6063/304SS joints (a) forge pressure of 30 MPa (b) forge pressure of 240 MPa [103].

specimens for AA 6063-304 SS, using a hemispherical bowl and thread of 1 mm pitch faying surfaces. Despite the faying modifications on the AA 6063 portion not improving strength, they encouraged bonding, resulting in better hardness. The bonding area increased as the hemispherical bowl-shaped faying surface had a U-shaped weld interface, thereby increasing joint efficiency [48]. Another study reported that tapering the faying surface of the SS304L specimen reduced friction time for sound weld joints and improved the AA 6061-304SS joint properties [9].

In another research, Pinheiro et al. [63] investigated the effects of using different initial contact geometry between aluminum ASTM A6351-T6 bars and SAE 1020 steel bars (Fig. 38). The results showed that a conical point of 60° exhibited a tensile strength increase of about 7.9% compared to the flat surface, and a bulged tip showed an increase of approximately 10.2%. The conical tips resulted in a higher average thickness of intermetallic layers, but its distribution was uniform, whereas flat tips had greater thicknesses and irregular distribution. The varying formation of intermetallic compounds is mainly due to heat distribution generated during friction. It is interesting to note that flat geometry fails to provide uniform force at the joint's interface, causing

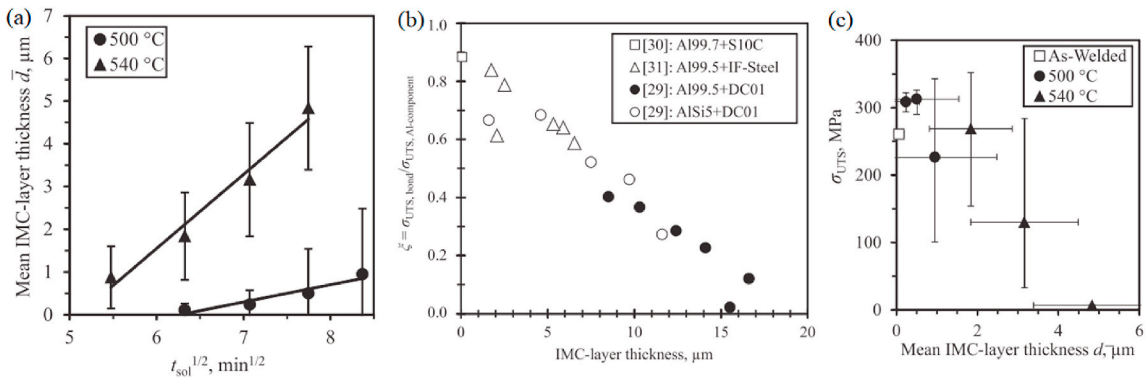

Fig. 37. (a) Mean IMC-layer-thickness over square root of time for two different solution annealing temperature, (b) ratio of ultimate tensile strength of the joint to the ultimate tensile strength of the aluminum over IMC layer thickness, (c) bond strength vs. IMC-layer thickness [60].

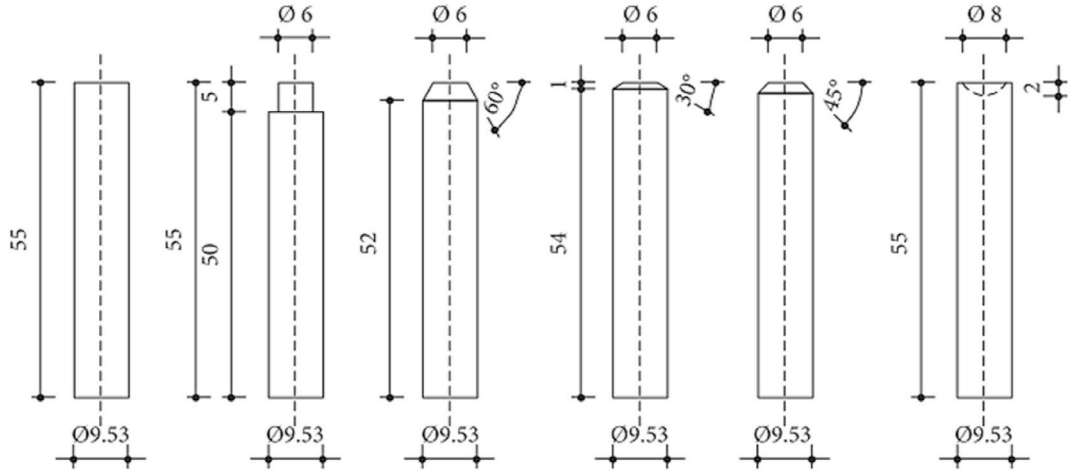

Fig. 38. Variation of the initial geometry of the used contact point of the aluminum pins [63].

the internal region to have a smaller force than the outside, which can trap oxides and other contaminants.

Additionally, it was discovered that shaping the steel surface into a V-shape resulted in a stronger bond between 6061 Al alloy and stainless steel [25]. The optimal geometry allowed for sufficient heat production and a path for IMCs to escape with material flow. The system with a 15° external taper displayed the highest joint strength due to efficient material flow and the expulsion of impurities and intermetallic compounds, resulting in a successful bond. Within the internal tapering system, the dynamically recrystallized zone was widest due to the heated-up aluminum alloy's inability to extrude easily [101].

One method to enhance the efficiency of welding metals together is to incorporate an interlayer. When connecting low alloy steel (AISI 4340) to aluminum (AA6061), silver interlayers were utilized and proved advantageous as they facilitated the formation and expansion of Fe_2Al_5 intermetallic. Implementing an electroplated silver interlayer on AISI 4340 deposited Si at the weld interface, substituting Mg at the AA6061 end; this diminished the width of the intermetallic compound layer and subsequently boosted tensile strength. Analysis of Fig. 39 shows that using the silver interlayer substitution of Fe–Al-based

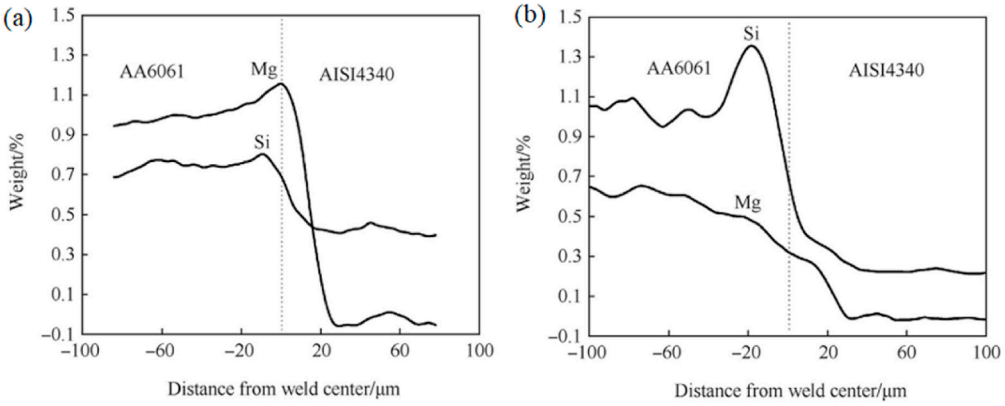

Fig. 39. Quantitative analysis across the weld interface for joint (a) without interlayer and (b) with silver interlayer [71].

intermetallic compounds with Ag–Al-based compounds arose at the interface. Since the Ag–Al phases are ductile, tensile strength did not decline. Additionally, in joints with silver interlayers, Si segregation at the weld interface on AA6061 restricted Fe diffusion and alleviated Fe–Al-based intermetallic formation-in its place, it is substituted with Al–Ag-based intermetallics like Ag_3Fe_2, Ag_2Al, and Ag_3Al; thus welds demonstrated better tensile strength and ductility [71]. This indicates that employing a silver interlayer mitigates the coefficient of friction, and the amount of heat generated, and lessens the softened zone's width at the AA6061- SS304 joint's bond line [104].

After friction welding AA6061 aluminum alloy with AISI 304 austenitic stainless steel, the resulting joints exhibited brittleness at a 0° bend angle due to Fe_2Al_5 formation. To address this, welding was conducted with interlayers containing Cu, Ni, and Ag as diffusion barrier layers, deposited through electroplating. However, welds with Cu and Ni interlayers proved brittle due to the presence of $CuAl_2$ and $NiAl_3$. Ag, on the other hand, acted as a reliable diffusion barrier and prevented Fe_2Al_5 formation. Consequently, welds with Ag interlayers exhibited superior strength and ductility, being bendable up to 100° (Fig. 40). The improved interlayer performance of Ag is due to the formation of ductile phases such as Ag_2Al and FeAl. This is because Fe had no solubility in Ag, thus enabling Ag to serve as an efficient diffusion barrier for Fe [77].

Another research investigated the use of SS 304 L alloy rods coated with three different metals (silver, nickel, and chromium) via electroplating, and then friction welded to AA6063 using various upset pressures (UP) of 18, 21, and 24 MPa. The results showed that the specimen with chromium electroplating exhibited the greatest welding performance, achieving a joint efficiency of 105% at 24 MPa, compared to the other coatings [105].

3.5. Al 7xxx series to steel joint

Directly joining A7075 to LCS via friction welding was difficult due to the risk of creating cracks in the A7075 flash. One approach to enhance the welding at the central area of the interface used a cone-shaped A7075 specimen, but it did not increase joint strength and produced low joint efficiency. Weaker joints with visible cracks in the flash of the A7075 side and extending to the interface appeared increasingly with higher forge pressure, as shown in Fig. 41 [106]. The crack in the A7075 flash seems to be a cause of poor plastic deformation ability. Therefore, to address this issue, pure Al (CP–Al) was used as an insert metal in the friction welding of A7075 and LCS. This method led to no cracks in the A7075 flash and resulted in a stronger joint [23].

The effects of friction welding parameters on the impact energy of welded joints between mild steel and aluminum alloy AA7075 were studied by Gupta et al. They found that the impact energy initially increased up to a certain point with increasing rotational speed and welding time. However, further increases in rotational speed and welding time decreased the impact energy. On the other hand, the impact energy continuously decreased with increasing workpiece diameter [107].

When AA 7020-T6 and SS 316 were joined together, significant

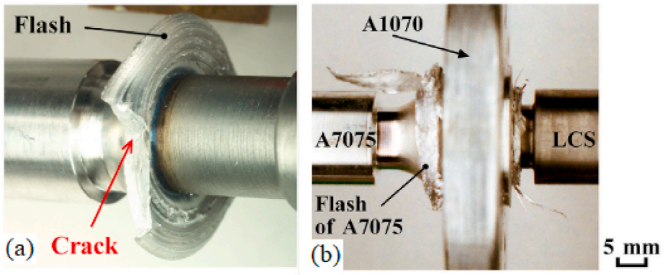

Fig. 41. Example of the appearance of joint; friction pressure of 36 MPa friction time of 6.5 s, and forge pressure of 180 MPa (a) without interlayer (b) with AA1070 interlayer [23].

tensile residual stresses were detected near the bond line on the AA7020 side. These stresses, inhomogeneously distributed from the perimeter to the rod center, were relatively high. On the other hand, high compressive residual stresses were found at the bond line in the center of 316L steel without any noticeable chemical or microscopic modifications in both materials [108].

4. Conclusions

Dissimilar Al-steel joints offer many benefits, including cost and weight reduction, and other unique properties. This has led to renewed interest in these joints across several industries, including automotive, aerospace, and marine sectors. However, creating dissimilar Al-steel systems is a challenging task given the complex nature of metallurgy involved. When creating Al-steel welds via friction-based methods, it's essential to minimize IMC interfacial reaction layers. These intermetallic compounds can reduce the ductility and toughness of the joints, making them susceptible to failure. The different types of intermetallic compounds can form at the interface of Al-St joints, such as Fe_2Al_5 and Fe_4Al_{13}.

To reduce the types and volume fraction of IMCs, various approaches can be used, including surface modification, interlayer material usage, heat input control, and post-weld heat treatment processes. This article provides a review of the friction welding process, including parameter influence, microstructural variations, IMC formation, and mechanical property variations in different Al-steel joints. The review shows that RFW can successfully address several of the challenges related to dissimilar Al-steel joints. The future of RFW looks bright, and ongoing developments in the field aim to improve joint quality and hybrid properties while building on the solid-state advantages of the technique. By identifying the factors that affect the joint properties practical recommendations for improving the joint quality can be interpreted.

Future outlook

The results of this study provide a valuable contribution to the understanding of the metallurgical characteristics of Al-St joints made by

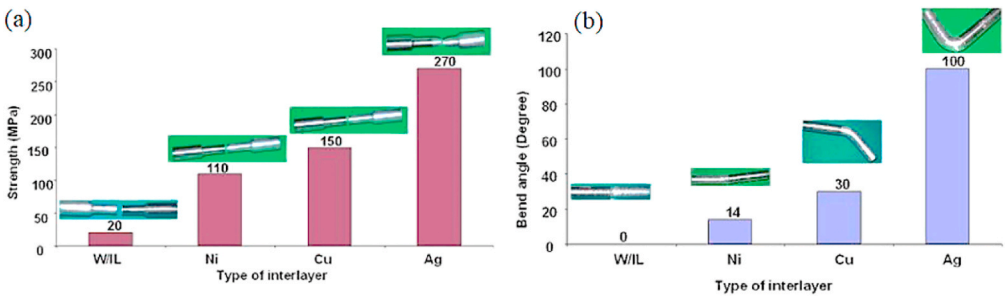

Fig. 40. Effect of interlayer on (a) tensile strength and (b) bend angle [77].

RFW. This knowledge can be used to improve the design and optimization of RFW processes for Al-St alloys. Specifically, the findings of this paper suggest that the following areas are promising for future research.

- The development of new strategies for preventing the formation of brittle intermetallic compounds in RFW of Al-St alloys. This could be achieved by optimizing the process parameters, such as the material preheating temperature and the modifying faying surface, or by using new materials or coatings.
- The study of the effects of RFW on the fatigue and corrosion properties of Al-St joints. This could help to ensure that the joints are strong and durable enough to withstand the harsh conditions of their intended application.
- The development of RFW processes for other new functional materials, such as High-Entropy Alloys (HEAs) alloys and composites.
- Development of new and improved joining technologies for a wide range of applications that are more efficient, reliable, and cost-effective.

In addition to the specific areas mentioned above, there are several other potential research directions that could be explored. For example, researchers could investigate the effects of RFW on the microstructure and mechanical properties of Al-St joints at different scales, such as the atomic microstructural levels. They could also study the effects of RFW on the environmental impact of Al-St joints, such as their recyclability and their potential to release harmful pollutants. Also, finite element method and various microstructure simulation procedures can be considered efficient and useful tools to reduce costs and time in rotary friction welding process design and optimization.

Declaration of competing interest

The authors declare that they have no known competing financial interests or personal relationships that could have appeared to influence the work reported in this paper.

Appendix

Process parameters and joint strength

The tensile strength vs. joint efficiency of different aluminum alloy-steel joints for the optimum welding parameters obtained from the literature is shown in Fig. 42.The joint efficiency is defined as the ratio of the overall joint strength to the strength of the weaker base metal, which is usually the aluminum alloy side. The results show that rotary friction welding has a relatively high joint efficiency for Al-Steel samples. The optimum parameters and other useful information for different aluminum-steel joint series were reviewed and presented in Table 3.

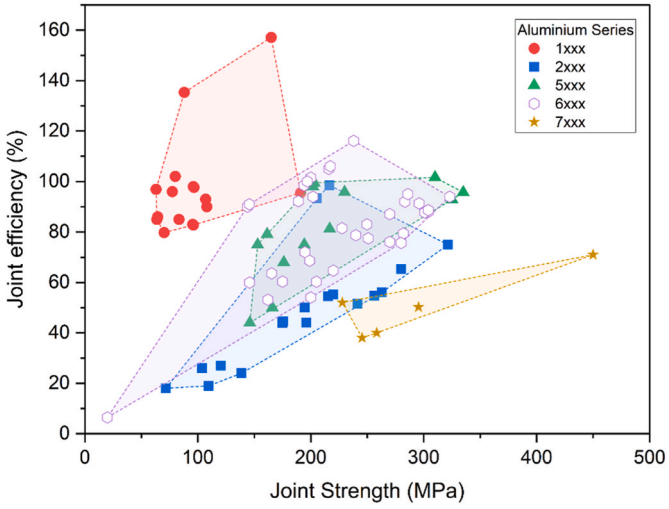

Fig. 42. Joint strength vs. joint efficiency of Al alloy/steel joints at optimum parameters with the results obtained from the literature.

Table 3
The optimal welding paramete

Al Series	Joint	Process Type	Optimum Welding Parameters						Tensile Strength of Joint (MPa)	Al BM Strength (MPa)	St BM Strength (MPa)	Joint eff. (%)	Remarks	Ref.
			Speed (RPM)	P_f (MPa)	t_f (s)	P_u (MPa)	t_u (s)	D (mm)						
1 xxx	AA 1070H-LCS	CDFW	1650	30	0.7	30	6	12	80	76	465	105	tempered condition	[82]
	AA 1060-Q235	CDFW	970	10	30	60		90	64	75	390	85	without interlayer	[24]
			970	10	30	60		90	65	75	390	86	with Ag interlayer	
	AA 1060-Q235	CDFW	1500	30	1	80	1	25	78	81	390	96	tilt angle external cone shape of 15°	[45]
	CP Al- AISI 304	CDFW	800	1.7	0.8	1.8	2	20	104				As-weld	[109]
	AA 1100-Mild Steel	CDFW	1000	5.2	1	49	1		178				As-weld	[110]
	CP Al-CP Fe	CDFW	1200	36	5				70	88		80	As-weld	[111]
	CP Al- AISI 304	CDFW	1650	30	1.5	150	6	12	108	120	670	90	As-weld	[84]
	Al 96 Zn1.1- AISI 304	CDFW	1410	30	4	60	12	10	191	200	825	96	As-weld	[3, 61]
	AA 1070- AISI 304	CDFW	2400	50	0.6	150	6	12	165	105		157	As-weld	[85]
	AA 1050- AISI 304	CDFW	300	2.1	32	1.4	2	14.8	80	78	355	102	As-weld	[8]
	AA 1050F-LCS	CDFW	1650	30	0.9	30		12	107	115	448	93	As-weld,	[81]
			1650	30	0.9	90		12	95	115	448	83	the joint by forge pressure of 90 MPa had hardly softened region	

Al Series	Joint	Process Type	Optimum Welding Parameters						Tensile Strength of Joint (MPa)	Al BM Strength (MPa)	St BM Strength (MPa)	Joint eff. (%)	Remarks	Ref.
			Speed (RPM)	P_f (MPa)	t_f (s)	P_u (MPa)	t_u (s)	D (mm)						
1 xxx	CP Al- IF steel	CDFW	2300	20	1	160	7	9.5	63	65		97	Preheat treatment to 1000 °C under a normal atmosphere	[62]
	CP Al - AISI 304	CDFW	2300	20	1	160	20	8	88	65		135	Preheat treatment to 1000 °C under an argon atmosphere	
	AA 1050- AISI 304	CDFW	2400	50	1.2	150	6	16	96	116	640	83	As-weld	[5, 58, 80, 112]
	AA 1050-H14-S25C	CDFW	3000	10	0.7	4		14	96	98	465	98	As-weld of solid bar	[79]
	AA 1050-H14-S25C		3000	10	0.7	4			83	98	465	85	As-weld of pipe joints	
2 xxx	AA 2219 T8- AISI 304	IFW	1300	160				15	242	469	878	52	Flat Surface	[87]
	AA 2219-T8- AISI 304	IFW	1300	160				15	257	469	878	55	hemispheric faying surface	[86]
			1300	160				15	263	469	878	56	tapering faying surface	
	2A14-T6 - AISI 304	IFW	1100	180				15	280	429		65	As-weld	[7]
	2A14-T6 - AISI 304	IFW	1100	180				15	322	429		75	As-weld	[16]

Al Series	Joint	Process Type	Optimum Welding Parameters						Tensile Strength of Joint (MPa)	Al BM Strength (MPa)	St BM Strength (MPa)	Joint eff. (%)	Remarks	Ref.
			Speed (RPM)	P_f (MPa)	t_f (s)	P_u (MPa)	t_u (s)	D (mm)						
	A2017-T4- AISI 1045	RFW	1800	14	60	42.1	40	15	175	399	667	44	As-weld	[88]
		LAFW	1800	21	60	42.1	40	15	220	399	667	55	Speed power of 1000 W	
	2A14 - AISI 304	IFW	1100	180				15	325				As-weld	[99]
	AA 2219-O- AISI 304	IFW	1100	120				15	206	220		93	As-weld	[113]
	AA 2017-T4-AISI 1045	IFW	1800	21				15	176	395	649	44	As-weld	[89]
		LAFW	1800	21				15	215	395	649	55	Speed power of 600 W	
2 xxx	AA 2219-AISI 304	CDFW	2000	116	5	193		18	217	220		99	As-weld	[114]
	AA 2011-T3-S25C	CDFW	3000	20	1	80		14	104	399	465	26	As-weld of solid bar	[79]
				20	1	80		14	72	399	465	18	As-weld of pipe joints	
	AA 2017-T4-S25C			30	4	60		14	196	446	465	44	As-weld of pipe joints	
				30	4	60		14	120	446	465	27	As-weld of pipe joints	
	AA 2024-T4-S25C			30	1.5	60		14	139	578	465	24	As-weld of solid bar	
	AA 2024-T4-S25C			30	1.5	60		14	110	578	465	19	As-weld of pipe joints	

Al Series	Joint	Process Type	Optimum Welding Parameters						Tensile Strength of Joint (MPa)	Al BM Strength (MPa)	St BM Strength (MPa)	Joint eff. (%)	Remarks	Ref.
			Speed (RPM)	P_f (MPa)	t_f (s)	P_u (MPa)	t_u (s)	D (mm)						
5 xxx	AA 5052- AISI 304	CDFW	1500	90		250		25	203	204	667	100	As-weld	[10]
			1500	90		250		25	161	204	667	79	PHWT at 250 °C for 20 min	
	AA 5052- AISI 304	CDFW	1500	90	1	250	15	20	153	204	667	75	As-weld	[92]
	AA 5052-S45C	CDFW	1200	40	1	230	6	19	335	350		96	As-weld	[94]
	AA 5052-S10C		1200	40	1	230	6	19	325	350		93		
	AA 5052-ASTM A36	CDFW	2000	70	0.5	137.5	5	20	202	206		98	As-weld	[93]
	AA 5052- AISI 304	CDFW	2400	50	1	150	6	16	230	240		96	As-weld	[6, 58]
	AA 5052- AISI 304	CDFW	2400	50	2	200	6	16	310	305		102	As-weld	[58]
	AA 5052-H34-S25C	CDFW	3000	25	0.8	62.5		14	194	259	465	75	As-weld of solid bar	[79]
			3000	25	0.8	62.5		14	176	259	465	68	As-weld of pipe joints	
	AA 5056-H34 -S25C	CDFW	3500	20	1.5	60		14	166	332	465	50	As-weld of solid bar	
			3500	20	1.5	60		14	146	332	465	44	As-weld of pipe joints	
6 xxx	AA6061-T6-AISI 304	IFW	1400	160				15					As-weld	[32]
	AA6061-T6-AISI 304	IFW	1100	160				15	282	355	890	79	As-weld	[25]

Al Series	Joint	Process Type	Optimum Welding Parameters						Tensile Strength of Joint (MPa)	Al BM Strength (MPa)	St BM Strength (MPa)	Joint eff. (%)	Remarks	Ref.
			Speed (RPM)	P_f (MPa)	t_f (s)	P_u (MPa)	t_u (s)	D (mm)						
6 xxx	AA6061-T6-AISI 304	IFW	1100	160				15	270	355	890	76	250 °C preheating	[25]
	AA6063-T6 - AISI 304L	CDFW	350	110	18	161	5	30.5	195	269	517	72	Pipe joints	[26]
	AA6063 - AISI 304L	CDFW	1300	18	5	24	3	12	238	205	515	116	hemispherical bowl and thread of 1 mm	[64]
	AA6061-T6-AISI 304	IFW	1100	160				15	200	370		54	As-machined	[102]
			1100	160				15	280	370		76	Polished	
	AA6061- AISI 304	CDFW	2000	40	1	220	10	15	304	346		88	As-weld	[115]
	AA6063-T6 - AISI 304L	CDFW	350	119	20	164.6	5	21.3	165	260	578	64	Pipe joints	[116]
	AA6063 - AISI 304L	CDFW	1300	18	5	24	3	12	216	205	515	105	Cr interlayer	[105]
	AA6063 - AISI 304L	CDFW	1500	18	3	21	3	12	217	205	515	106	tapering surface	[9]
	AA6061-T6- AISI 304	CDFW	2000	20.38	10	21.74	7	25	179				As-weld	[117]
	AA6063 - AISI 304L	CDFW	1300	18	5	24	3	12	189	205	485	92	As-weld	[118]
	AA6061-AISI 304	CDFW	2200	40	12	220	12	15	304	343		89	As-weld	[96]
		IFW	1100	180				15	323	343		94	As-weld	
	AA6061- AISI 304	CDFW	2200	40	4	220	8	15	301	343		88	As-weld	[119]
	AA6063 - AISI 304	CDFW	1650	30	1.5	240	6	16	200	197	663	102	As-weld	[103]

Al Series	Joint	Process Type	Optimum Welding Parameters						Tensile Strength of Joint (MPa)	Al BM Strength (MPa)	St BM Strength (MPa)	Joint eff. (%)	Remarks	Ref.
			Speed (RPM)	P_f (MPa)	t_f (s)	P_u (MPa)	t_u (s)	D (mm)						
6 xxx	AA6063 - AISI 304	CDFW	1650	30	1.5	30	6	16	194	197	663	98	PWHT at 473 k, 3.6 ks	[103]
	A6351-T6 - SAE 1020	CDFW	1750	21.63	4	21.63	6	9.53	175	290	420	60	As-weld	[63]
			1750	21.63	4	21.63	6	9.53	199	290	420	69	bulged tip surface	
	AA 6061-T6-AISI 304	IFW	1100	180				15	323	343		94	As-weld	[11]
	AA 6061-T6-AISI 304	CDFW	2200	40	4	220	8	15	304	343		89	As-weld	[120]
	AA 6061- AISI 316L	CDFW	580	51.26	29	152	80		166				15° welding groove	[18]
	AA 6063 - AISI 304	CDFW	1650	30	1.5	240	6	12	197	197	670	100	As-weld	[20]
	AA 6082-20MnCr5	CDFW	700	130		170		30	261				As-weld	[60]
	AA 6082-20MnCr5	CDFW	700	130		170		30	313				PWHT at 500°C and 1 hr.	
	AA 6063-H18 - AISI 304	CDFW	1650	30	0.4	135	6	6.7	146	243	770	60	Pipe joints	[95]
	AA 6082-T6-AISI 1040	CDFW		90	4	180		10	220				As-weld	[121]
	AA 6061-T6- AISI 4340 QT	CDFW	2400	15		30		16	162	305	1100	53	As-weld	[71]
			2400	15		30		16	240	305	1100	79	with Ag interlayer	
	AA 6061- AISI 304	CDFW	1500	45		115	3		205	340	605	60	As-weld	[101]

Al Series	Joint	Process Type	Optimum Welding Parameters						Tensile Strength of Joint (MPa)	Al BM Strength (MPa)	St BM Strength (MPa)	Joint eff. (%)	Remarks	Ref.
			Speed (RPM)	P_f (MPa)	t_f (s)	P_u (MPa)	t_u (s)	D (mm)						
6 xxx	AA 6061- AISI 304	CDFW	1500	45		115	3		220	340	605	65	External Taper 15°	[101]
	AA 6082 - AISI 304	CDFW	1400	104	5	210	6	14	188				As-weld	[122]
	AA 6061-T6- AISI 1018	IFW	4200	23	1	60	5	12.5	250				As-weld	[19]
	AA6061- AISI 304	CDFW	1500	24		146		16	202	215	515	94	As-weld	[4]
	AA 6061- AISI 304	CDFW	2400	11.8		23.6		18	20	310	580	6	As-weld	[77]
			2400	11.8		23.6		18	270	310	580	87	with Ag interlayer	
	AA 6061- S45C	CDFW	4000	19.1	1	296.5	10		283	308		92	As-weld	[123]
	AA 6061- AISI 304	CDFW	3500	30	1	260	10	13	251	324	711	77	Tensile at a loading rate of 20	[124]
	AA 6061- AISI 304	CDFW	3500	30	2	260	10	13	296	324	711	91	at 4×10^6 (MPa/s)	
	AA 6061-T6-S25C	CDFW	3000	30	1	180		14	286	301	465	95	As-weld of solid bar	[79]
				30	1	180		14	250	301	465	83	As-weld of pipe joints	
	AA 6063-T5-S25C			20	1	80		14	144	160	465	90	As-weld of solid bar	

Al Series	Joint	Process Type	Optimum Welding Parameters						Tensile Strength of Joint (MPa)	Al BM Strength (MPa)	St BM Strength (MPa)	Joint eff. (%)	Remarks	Ref.
			Speed (RPM)	P_f (MPa)	t_f (s)	P_u (MPa)	t_u (s)	D (mm)						
6 xxx	AA 6063-T5-S25C	CDFW	3000	20	1	80		14	146	160	465	91	As-weld of pipe joints	[79]
7 xxx	AA 7075-T6-LCS	CDFW	1650	36	6.5	450	10	10	450	642	439	71	Using Pure AA1070 interlayer	[23]
	AA 7075-T6-LCS	CDFW	1650	30	3	180	6	12	228	642	439	52	As-weld: Cracks were observed with a forge pressure of 180 MPa or higher	[106]
	AA 7075-T6-S25C	CDFW	3000	30	2	60		14	245	646	465	38	As-weld of solid bar	[79]
			3000	30	2	60		14	258	646	465	40	As-weld of pipe joints	

Artificial neural network analysis on joint strength

The multi-layer perceptron (MLP) is a powerful artificial neural network (ANN) architecture that falls under the umbrella of both artificial intelligence and machine learning. It is particularly well-suited for regression modeling of complex processes, such as the rotary friction welding process [109]. The MLP consists of multiple layers of interconnected artificial neurons, allowing it to capture intricate relationships between input variables and output responses. By training the MLP on a dataset of input-output pairs, it learns to approximate the underlying mapping between the input variables (e.g., welding parameters) and the desired output (e.g., weld quality or strength). This makes the MLP an effective tool for regression modeling in the welding process, enabling engineers and researchers to predict and optimize key process parameters to achieve desired outcomes [110].

In this section, the relationship between the welding strength of steel to aluminum joint and various input parameters was modeled using a Multi-Layer Perceptron Artificial Neural Network method and the results were presented. The data used for this model was collected by using pertinent articles and research in the field of FRW of steel to aluminum. The data included different kinds of aluminum series as well as various kinds of carbon and stainless steel.

The ANN architecture consisted of a hidden layer with 9 neurons, employing the Tansig transfer function, and an output layer with a linear transfer function, as shown in Fig. 43. The network was trained using a Levenberg-Marquardt method to learn the complex relationship between the input parameters and the strength of the welding. The input parameters considered in this model encompassed both process-related and material-related factors. Process-related parameters included friction and forging pressure and times, rotation speed, and diameter of the weldment. Material parameters comprised the friction coefficient, μ, yield strength, *Ys,* and material heat transfer parameters such as thermal conductivity, k, heat capacity, C_p, and density, ρ. To simplify and reduce the number of input parameters and, also, to improve the efficiency of the model, certain parameters were

integrated. The thermal parameters, represented by the thermal diffusivity coefficient, α, and the material heat generation coefficient, φ, were represented by a combination of the yield strength, diameter, D, friction coefficient, and rotational speed, ω, to form a composite set of heat generation according to previous works, which are presented in equations (4) and (5) [111–114].

$$\alpha = \frac{k}{\rho\, C_p} \tag{4}$$

$$\begin{cases} \varphi_i = \mu.Y_s.D.\omega \\ \varphi = \varphi_{Al} + \varphi_{St} \end{cases} \tag{5}$$

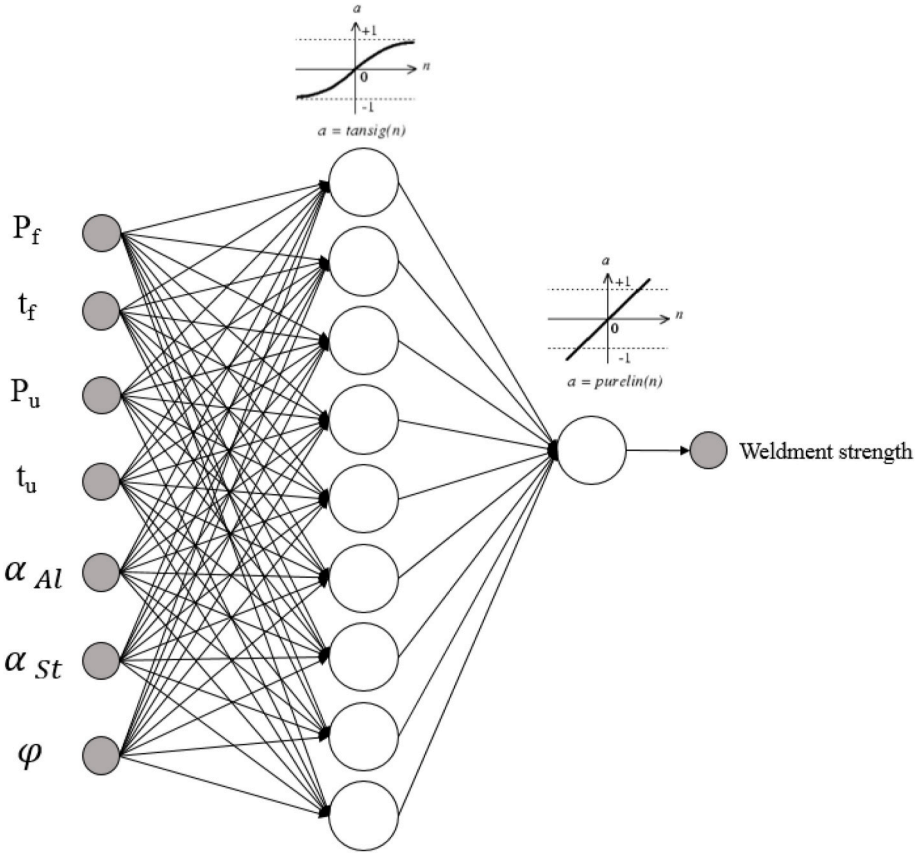

Fig. 43. MLP ANN Structure in prediction of Al-Steel joint strength.

By obtaining the appropriate ANN model, the relationship between bond strength with friction pressure and forging pressure for various alloys of aluminum with stainless steel was obtained in the form of contour plots. The developed model allowed for the creation of contour plots illustrating how friction pressure and forging pressure affected the final strength of the weld. These contours were generated while keeping the rotational speed, friction time, and upset time fixed, 1500 RPM, 4 s, and 6 s, respectively. Also, the connection between different grades of aluminum and stainless steel 304 was examined, as shown in fig. 44.

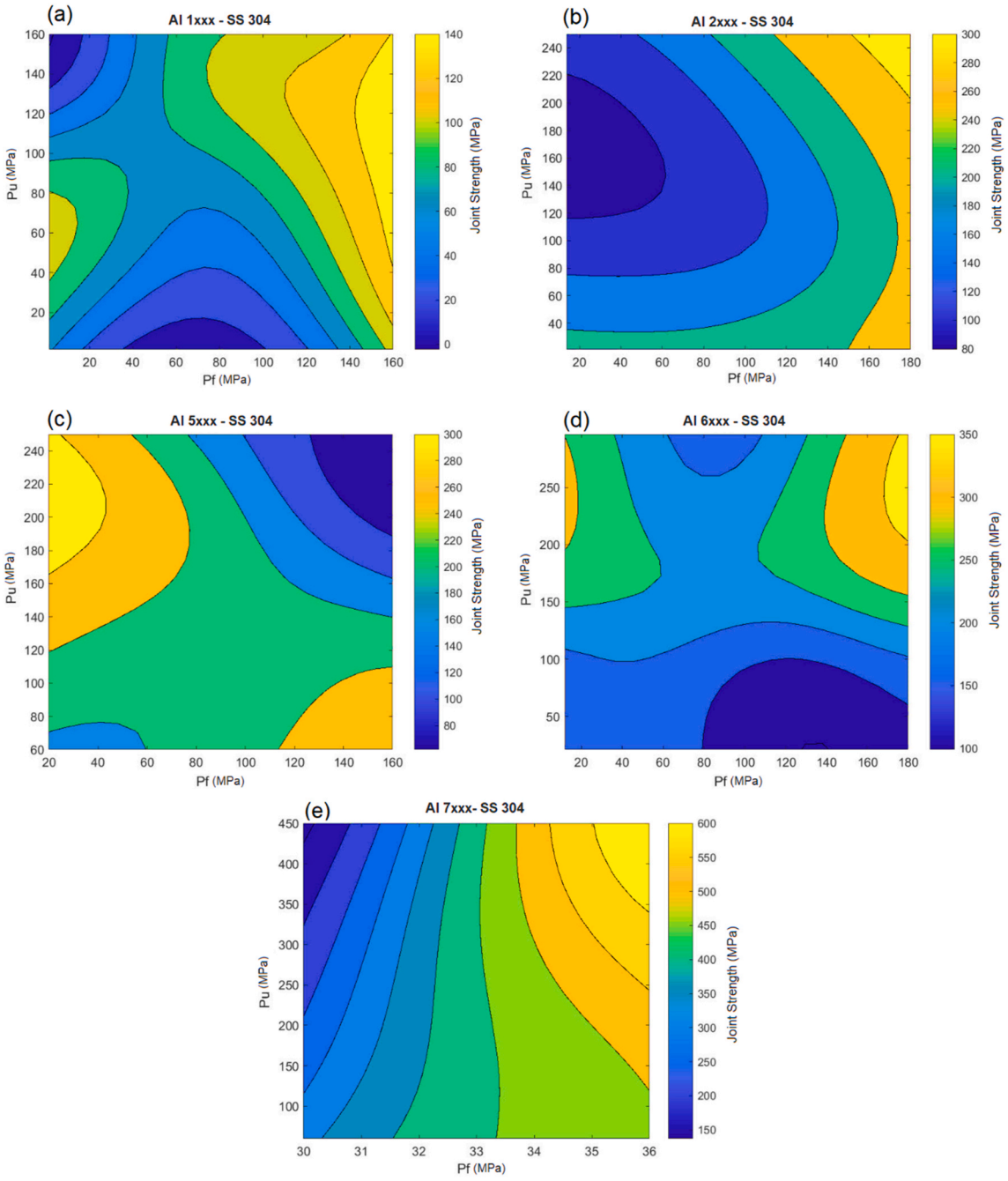

Fig. 44. MLP-ANN results for joint strength of SS 304 to aluminum alloy series (a) 1xxx (b) Al 2xxx (c) Al 5xxx (d) Al 6xxx (e) Al 7xxx.

By analyzing the MLP-ANN results based on the data from the reviewed literature, the following conclusions can be drawn:

For the AA 1xxx series in connection with 304 stainless steel, the low frictional pressure causes insufficient element diffusion and a weak metallurgical bonding effect, which lowers the joint strength relative to the aluminum side base metal. As illustrated in fig. 44a, an increase in friction pressure causes the element diffusion distance to increase, resulting in the formation of more brittle and hard intermetallic compounds. When these compounds are overly thick, they negatively affect the bonding qualities. Diffusion is responsible for the increase in IMC thickness, since the intermetallic interlayer's thickness is dependent on both friction pressure and friction time. Furthermore, it is believed that an increased friction pressure may have caused the reaction layer to discharge in a flash. Hence, there may be an improvement in joint strength.

Regarding the AA 2xxx series to 304 stainless steel joints, lower ductility alloys require less upset to produce a sound weld. This is because a good bond requires less material to be displaced. Al-2xxx series alloys, for example, have lesser ductility than Al-5xxx series alloys. The best welding parameter combination for obtaining high-quality welded joints at medium pressure was discovered to be low upset pressure and higher friction pressure, as shown in fig. 44b.

In the case of AA 5xxx series in joining with 304 stainless steel, when magnesium is present in large concentrations, obstructs joining. However, it has a low content in AA 5052 and 6xxx series alloys, resulting in good friction weldability, similar to pure aluminum. A5056 has a relatively high magnesium concentration, which results in a thick brittle intermetallic compound layer and slightly inferior friction weldability. As a result, decreased

friction pressure leads to less thermal diffusion and IMC formation, as seen in fig. 44c. On the other hand, the short friction time results in insufficient frictional heat, and the oxide film removal at the weld interface and inter-diffusion of the components of both metals become insufficient. As a result, even with higher upset pressure, the remaining non-bonded zones must be monitored.

Considering the AA 6xxx series and 304 stainless steel joints, fig. 44dshows the increased joint strength with increasing upset pressure. No defect likely develops at the interface when the friction duration is minimal and the upset pressure is large. The metallurgical bonding may be realized even if the IMCs layer does not form at the contact; instead, a thin diffusion zone may occur. The presence of magnesium in AA6061 close to the interface is thought to promote the growth and formation of the Fe_2Al_5 intermetallic and result in low tensile strength at high heat input. This can be connected to the various joint residual stress distributions. As a result, the formation of nanoscale interfacial microstructures is preferred to produce joints with high strength. The upset pressure is roughly correlated with the joint's tensile strength. Excessive frictional pressure generates a lot of heat, causing significant softening of the HAZ on the Al side and lowering the tensile strength of the joint. As a result, a high upset pressure and an appropriate friction pressure are required.

About the joining of 304 stainless steel and AA 7xxx series, higher-strength alloys need greater axial force to produce a sound weld. Since stronger bonding and plastic deformation of the material require greater force. Al-7xxx series alloys, for instance, are stronger than Al-1xxx series alloys. Conversely, if the joint is formed under high upset pressure, it probably has low tensile strength because the A7075 flash cracks due to the base metal's poor plastic deformation ability. Therefore, it may be concluded from fig. 44ethat comparatively low pressure enhances joint strength.

References

[1] Mehta KP. A review on friction-based joining of dissimilar aluminum–steel joints. J Mater Res 2019;34(1):78–96. https://doi.org/10.1557/jmr.2018.332.

[2] Hincapié OD, Salazar JA, Restrepo JJ, Graciano-Uribe JA, Torres EAJEJ. Weldability of aluminum-steel joints using continuous drive friction welding process, without the presence of intermetallic compounds 2020;24(1):129–44. https://doi.org/10.4186/ej.2020.24.1.129.

[3] Sahin M. Joining of stainless-steel and aluminium materials by friction welding. Int J Adv Manuf Technol 2009;41(5–6):487–97. https://doi.org/10.1007/s00170-008-1492-7.

[4] Sammaiah P, Suresh A, Tagore G. Mechanical properties of friction welded 6063 aluminum alloy and austenitic stainless steel. J Mater Sci 2010;45(20):5512–21. https://doi.org/10.1007/s10853-010-4609-y.

[5] Fukumoto S, Tsubakino H, Okita K, Aritoshi M, Tomita T. Microstructure of friction weld interface of 1050 aluminium to austenitic stainless steel. J Mater Sci Technol 1998;14(4):333–8. https://doi.org/10.1179/mst.1998.14.4.333.

[6] Fukumoto S, Tsubakino H, Okita K, Aritoshi M, Tomita T. Friction welding process of 5052 aluminium alloy to 304 stainless steel. J Mater Sci Technol 1999;15(9):1080–6. https://doi.org/10.1179/026708399101506805.

[7] Zhang D, Qin G, Ma H, Geng P. Non-uniformity of intermetallic compounds and properties in inertia friction welded joints of 2A14 Al alloy to 304 stainless steel. J Manuf Process 2021;68:834–42. https://doi.org/10.1016/j.jmapro.2021.06.019.

[8] Alves EP, Piorino Neto F, An CY. Welding of AA1050 aluminum with AISI 304 stainless steel by rotary friction welding process. J Aerosp Technol 2010;2(3):301–6. https://doi.org/10.5028/jatm.2010.02037110.

[9] Senthil Murugan S, Noorul Haq A, Sathiya P. Effect of welding parameters on the microstructure and mechanical properties of the friction-welded dissimilar joints of AA6063 alloy and faying surface-tapered AISI304L alloy. Weld World 2020. https://doi.org/10.1007/s40194-020-00846-x.

[10] Dong H, Yang J, Li Y, Xia Y, Hao X, Li P, et al. Evolution of interface and tensile properties in 5052 aluminum alloy/304 stainless steel rotary friction welded joint after post-weld heat treatment. J Manuf Process 2020;51:142–50. https://doi.org/10.1016/j.jmapro.2020.01.038.

[11] Liu Y, Zhao H, Peng Y, Ma X. Mechanical properties of the inertia friction welded aluminum/stainless steel joint. Weld World 2019;63(6):1601–11. https://doi.org/10.1007/s40194-019-00793-2.

[12] Yang Y, Luo Z, Zhang Y, Su J. Dissimilar welding of aluminium to steel: a review. J Manuf Process 2024;110:376–97. https://doi.org/10.1016/j.jmapro.2023.12.060.

[13] Xu Y, Liu Q, Xu J, Xiao R, Chen S. Review on multi-information acquisition, defect prediction and quality control of aluminum alloy GTAW process. J Manuf Process 2023;108:624–38. https://doi.org/10.1016/j.jmapro.2023.11.025.

[14] Rafi HK, Ram GJ, Phanikumar G, Rao KP. Microstructure and tensile properties of friction welded aluminum alloy AA7075-T6. Mater Des 2010;31(5):2375–80. https://doi.org/10.1016/j.matdes.2009.11.065 (1980-2015).

[15] Zhang C, Li H, Liu Q, Huang C, Zhou K. Ultrasonic welding of aluminum to steel: a review. Metals 2023;13(1). https://doi.org/10.3390/met13010029.

[16] Zhang D, Qin G, Geng P, Ma H. Study of plastic flow on intermetallic compounds formation in friction welding of aluminum alloy to stainless steel. J Manuf Process 2021;64:20–9. https://doi.org/10.1016/j.jmapro.2021.01.019.

[17] Wan L, Huang Y. Friction stir welding of dissimilar aluminum alloys and steels: a review. Int J Adv Manuf Technol 2018;99(5):1781–811. https://doi.org/10.1007/s00170-018-2601-x.

[18] Wan L, Huang Y. Friction welding of AA6061 to AISI 316L steel: characteristic analysis and novel design equipment. Int J Adv Manuf Technol 2018;95(9–12):4117–28. https://doi.org/10.1007/s00170-017-1505-5.

[19] Taban E, Gould JE, Lippold JC. Dissimilar friction welding of 6061-T6 aluminum and AISI 1018 steel: properties and microstructural characterization. Mater Des 2010;31(5):2305–11. https://doi.org/10.1016/j.matdes.2009.12.010 (1980-2015).

[20] Kimura M, Suzuki K, Kusaka M, Kaizu K. Effect of friction welding condition on joining phenomena and mechanical properties of friction welded joint between 6063 aluminium alloy and AISI 304 stainless steel. J Manuf Process 2017;26:178–87. https://doi.org/10.1016/j.jmapro.2017.02.008.

[21] Patel MM, Badheka VJ. A review on friction stir welding (FSW) process for dissimilar aluminium to steel metal systems. Weld Int 2024;38(2):91–115. https://doi.org/10.1080/09507116.2023.2291064.

[22] Sharma C, Tripathi A, Upadhyay V, Verma V, Sharma SK. Friction stir spot welding-process and weld properties: a review. J Inst Eng: Series D 2021;102(2):549–65. https://doi.org/10.1007/s40033-021-00276-z.

[23] Kimura M, Kusaka M, Kaizu K, Hayashida K. Simultaneous friction welding and characterization of joints between 7075-T6 al alloy and low-carbon steel using pure Al as an insert metal. J Mater Eng Perform 2019;28(12):7726–36. https://doi.org/10.1007/s11665-019-04507-z.

[24] Zhang C, Cui G, Chen B, Liu X, Shi Y, Wang Y. Effect of Ag interlayer on friction torque, mechanical properties and microstructure of large diameter aluminum/steel joints by continuous drive friction welding. J Manuf Process 2022;78:341–51. https://doi.org/10.1016/j.jmapro.2022.04.006.

[25] Ma H, Qin G, Dang Z, Qu S, Chen L, Geng P. Interfacial microstructure evolution and mechanical properties of inertia friction welded aluminium alloy/stainless steel joint with preheat treatment. Mater Sci Eng A 2022;836:142671. https://doi.org/10.1016/j.msea.2022.142671.

[26] Vyas HD, Mehta KP, Badheka V, Doshi B. Processing and evaluation of dissimilar Al-SS friction welding of pipe configuration: nondestructive inspection, properties, and microstructure. Meas 2021;167:108305. https://doi.org/10.1016/j.measurement.2020.108305.

[27] Wallerstein D, Salminen A, Lusquiños F, Comesaña R, García JV, Rodríguez AR, et al. Recent developments in laser welding of aluminum alloys to steel. Metals 2021;11(4). https://doi.org/10.3390/met11040622.

[28] Yang J, Oliveira JP, Li Y, Tan C, Gao C, Zhao Y, et al. Laser techniques for dissimilar joining of aluminum alloys to steels: a critical review. J Mater Process Technol 2022;301. https://doi.org/10.1016/j.jmatprotec.2021.117443.

[29] Liu Y, Li F, Li Y, Zhu Z, Chen H. Evolution mechanism of interfacial microstructure and regulation of mechanical properties of laser-arc hybrid weld-brazing aluminum/steel joints under different post-welding heat-treatment temperatures. J Mater Res Technol 2024;29:933–49. https://doi.org/10.1016/j.jmrt.2024.01.168.

[30] Norouzian M, Amne Elahi M, Plapper P. A review: suppression of the solidification cracks in the laser welding process by controlling the grain structure and chemical compositions. J Adv Join Process 2023;7:100139. https://doi.org/10.1016/j.jajp.2023.100139.

[31] Singh J, Arora KS, Shukla DK. Dissimilar MIG-CMT weld-brazing of aluminium to steel: a review. J Alloys Compd 2019;783:753–64. https://doi.org/10.1016/j.jallcom.2018.12.336.

[32] Ma H, Zhao Y, Qin G, Geng P. Formation of nanoscale reaction layer with several crystallinities in the friction-welded 6061 Al alloy/steel joint. Mater Des 2022;219:110742. https://doi.org/10.1016/j.matdes.2022.110742.

[33] A review on advances in friction welding of dissimilar metals. In: Gill D, Pradhan MK, editors. International conference on advances in mechanical engineering and material science. Singapore: Springer Nature Singapore; 2022 Apr 22.

[34] Kalyankar V, Chudasama G. On the metallurgical challenges of intermetallic compound in steel/Al dissimilar resistance spot welding: significance, growth and controlling mechanisms. Adv Mater Process Technol 2023. https://doi.org/10.1080/2374068X.2023.2206175.

[35] Wang J, Fu X, Zhang L, Zhang Z, Liu J, Chen S. A short review on laser welding/brazing of aluminum alloy to steel. Int J Adv Manuf Technol 2021;112(9–10):2399–411. https://doi.org/10.1007/s00170-021-06607-4.

[36] Ambroziak A, Korzeniowski M, Kustroń P, Winnicki M, Sokołowski P, Harapińska E. Friction welding of aluminium and aluminium alloys with steel. Adv Mater Sci Eng 2014;2014. https://doi.org/10.1155/2014/981653.

[37] Haghshenas M, Gerlich AP. Joining of automotive sheet materials by friction-based welding methods: a review. Eng Sci Technol Int 2018;21(1):130–48. https://doi.org/10.1016/j.jestch.2018.02.008.

[38] Beygi R, Galvão I, Akhavan-Safar A, Pouraliakbar H, Fallah V, da Silva LFM. Effect of alloying elements on intermetallic formation during friction stir welding of dissimilar metals: a critical review on aluminum/steel. Metals 2023;13(4). https://doi.org/10.3390/met13040768.

[39] Hussein SA, Tahir ASM, Hadzley AB. Characteristics of aluminum-to-steel joint made by friction stir welding: a review. Mater Today Commun 2015;5:32–49. https://doi.org/10.1016/j.mtcomm.2015.09.004.

[40] Uday M, Ahmad Fauzi M, Zuhailawati H, Ismail A. Advances in friction welding process: a review. Sci Technol Weld 2010;15(7):534–58. https://doi.org/10.1179/136217110X12785889550064.

[41] Kumar Rajak D, Pagar DD, Menezes PL, Eyvazian A. Friction-based welding processes: friction welding and friction stir welding. J Adhes Sci. 2020;34(24):2613–37. https://doi.org/10.1080/01694243.2020.1780716.

[42] Maalekian M. Friction welding–critical assessment of literature. Sci Technol Weld 2007;12(8):738–59. https://doi.org/10.1179/174329307X249333.

[43] Sathishkumar GB, Sethuraman P, Chanakyan C, Sundaraselvan S, Joseph Arockiam A, Alagarsamy SV, et al. Friction welding of similar and dissimilar materials: a review. Mater Today Proc 2021. https://doi.org/10.1016/j.matpr.2021.03.089.

[44] Li W, Vairis A, Preuss M, Ma T. Linear and rotary friction welding review. Int Mater Rev 2016;61(2):71–100. https://doi.org/10.1080/09506608.2015.1109214.

[45] Zhang C, Wang S, Luo D, Shi W, Liu X, Cui G, et al. Study of the mechanical properties and microstructures of conical joints for aluminum/steel continuous drive friction welding. J Manuf Process 2021;67:241–52. https://doi.org/10.1016/j.jmapro.2021.04.070.

[46] Maalekian M, Kozeschnik E, Brantner HP, Cerjak H. Comparative analysis of heat generation in friction welding of steel bars. Acta Mater 2008;56(12):2843–55. https://doi.org/10.1016/j.actamat.2008.02.016.

[47] Li W, Wen Q, Yang X, Wang Y, Gao D, Wang W. Interface microstructure evolution and mechanical properties of Al/Cu bimetallic tubes fabricated by a novel friction-based welding technology. Mater Des 2017;134:383–93. https://doi.org/10.1016/j.matdes.2017.08.065.

[48] Rao M, Hazlett T. A study of the mechanisms involved in friction welding of aluminum alloys. Weld J 1970;49(4):1815–85.

[49] Ajay V, Babu NK, Ashfaq M, Kumar TM, Krishna KV. A review on rotary and linear friction welding of inconel alloys. Trans Indian Inst Met. 2021;74(11):2583–98. https://doi.org/10.1007/s12666-021-02345-z.

[50] Winiczenko R, Goroch O, Krzyńska A, Kaczorowski M. Friction welding of tungsten heavy alloy with aluminium alloy. J Mater Process Technol 2017;246:42–55. https://doi.org/10.1016/j.jmatprotec.2017.03.009.

[51] Kimura M, Inoue H, Kusaka M, Kaizu K, Fuji A. Analysis method of friction torque and weld interface temperature during friction process of steel friction welding. J Solid Mech Mater Eng 2010;4(3):401–13. https://doi.org/10.1299/jmmp.4.401.

[52] Dang Z, Qin G, Guo X. Formation and growth mechanism of Cu-rich layer at aluminum/steel friction welding interface. J Mater Res Technol 2023;27:35–47. https://doi.org/10.1016/j.jmrt.2023.09.285.

[53] Pan B, Sun H, Shang S-L, Banu M, Wang P-C, Carlson BE, et al. Understanding formation mechanisms of intermetallic compounds in dissimilar Al/steel joint processed by resistance spot welding. J Manuf Process 2022;83:212–22. https://doi.org/10.1016/j.jmapro.2022.08.062.

[54] He H, Gou W, Wang S, Hou Y, Ma C, Mendez PF. Kinetics of intermetallic compound layers during initial period of reaction between mild steel and molten aluminum. Int J Mater Res 2019;110(3):194–201. https://doi.org/10.3139/146.111735.

[55] Sawai T, Ogawa K, Yamaguchi H, Ochi H, Yamamoto Y, Suga Y. Evaluation of joint strength of friction welded carbon steel by heat input. Weld Int 2002;16:432–41. https://doi.org/10.1080/09507110209549556.

[56] Li X, Li J, Jin F, Xiong J, Zhang F. Effect of rotation speed on friction behavior of rotary friction welding of AA6061-T6 aluminum alloy. Weld World 2018:1–8. https://doi.org/10.1007/s40194-018-0601-y.

[57] Atabaki MM, Nikodinovski M, Chenier P, Ma J, Harooni M, Kovacevic R. Welding of aluminum alloys to steels: an overview. J Manuf Sci Prod 2014;14(2):59–78. https://doi.org/10.1515/jmsp-2014-0007.

[58] Fukumoto S, Tsubakino H, Okita K, Aritoshi M, Tomita T. Static joint strength of friction welded joint between aluminium alloys and stainless steel. Weld Int 2000;14(2):89–93. https://doi.org/10.1080/09507110009549145.

[59] Taban E, Gould JE, Lippold JC. Characterization of 6061-T6 aluminum alloy to aisi 1018 steel interfaces during joining and thermo-mechanical conditioning. Mater Sci Eng A 2010;527(7):1704–8. https://doi.org/10.1016/j.msea.2009.10.059.

[60] Herbst S, Aengeneyndt H, Maier HJ, Nürnberger F. Microstructure and mechanical properties of friction welded steel-aluminum hybrid components after t6 heat treatment. Mater Sci Eng A 2017;696:33–41. https://doi.org/10.1016/j.msea.2017.04.052.

[61] Sahin M. Characterization of properties in friction-welded austenitic-stainless steel and aluminium joints. Ind Lubric Tribol 2014;66(2):260–71. https://doi.org/10.1108/ILT-11-2011-0100.

[62] Yılmaz M, Çöl M, Acet M. Interface properties of aluminum/steel friction-welded components. Mater Charact 2002;49(5):421–9. https://doi.org/10.1016/S1044-5803(03)00051-2.

[63] Pinheiro MA, Bracarense AQ. Influence of initial contact geometry on mechanical properties in friction welding of dissimilar materials aluminum 6351 T6 and SAE 1020 steel. Adv Mater Sci Eng 2019;2019. https://doi.org/10.1155/2019/1759484.

[64] Subramanian SM, Paulraj S, Abdul Haq NH. Effect of faying surfaces and characterization of aluminium AA6063–steel AISI304l dissimilar joints fabricated by friction welding with hemispherical bowl and threaded faying surfaces. Int J Adv Manuf Technol 2021;116(1–2):629–66. https://doi.org/10.1007/s00170-021-07445-0.

[65] Cheepu M, Che WS. Friction welding of titanium to stainless steel using al interlayer. Trans Indian Inst Met. 2019;72(6):1563–8. https://doi.org/10.1007/s12666-019-01655-7.

[66] Kumar R, Balasubramanian M. Experimental investigation of Ti–6Al–4V titanium alloy and 304L stainless steel friction welded with copper interlayer. Def Technol 2015;11(1):65–75. https://doi.org/10.1016/j.dt.2014.10.001.

[67] Cheepu M, Ashfaq M, Muthupandi V. A new approach for using interlayer and analysis of the friction welding of titanium to stainless steel. Trans Indian Inst Met. 2017;70(10):2591–600. https://doi.org/10.1007/s12666-017-1114-x.

[68] Reddy MG, Rao SA, Mohandas T. Role of electroplated interlayer in continuous drive friction welding of AA6061 to AISI 304 dissimilar metals. Sci Technol Weld Join 2008;13(7):619–28. https://doi.org/10.1179/174329308X319217.

[69] Velu PS, Hynes NRJ, Vignesh NJ. Joining of AA 6061/Ti–6Al–4V with zinc interlayer using friction welding process. J Braz Soc Mech Sci Eng 2019;41(12). https://doi.org/10.1007/s40430-019-2029-8.

[70] Kim HJ, Hong SI. Effect of Ni interlayer on the interface toughening and thermal stability of Cu/Al/Cu clad composites. Met Mater Int 2019;25(1):94–104. https://doi.org/10.1007/s12540-018-0170-z.

[71] Meshram SD, Madhusudhan Reddy G. Friction welding of AA6061 to AISI 4340 using silver interlayer. Def Technol 2015;11(3):292–8. https://doi.org/10.1016/j.dt.2015.05.007.

[72] Teker T, Karakurt EM. Examination of mechanical properties of high chromium white cast iron/AISI1030 steel welded by friction welding with nickel interlayer. Sci Technol Weld 2019. https://doi.org/10.1080/13621718.2019.1648720.

[73] Balasubramanian M, Kumar R, Gopinath S. Multi-objective optimisation of friction welding parameters in joining titanium alloy and stainless steel with a novel interlayer geometry. Adv Mater Process Technol 2020;6(1):25–39. https://doi.org/10.1080/2374068X.2019.1688625.

[74] Fukumoto S, Inoue T, Mizuno S, Okita K, Tomita T, Yamamoto A. Friction welding of TiNi alloy to stainless steel using Ni interlayer. Sci Technol Weld 2010;15(2):124–30. https://doi.org/10.1179/136217109X12577814486692.

[75] Seli H, Noh MZ, Ismail Ai Md, Rachman E, Ahmad ZA. Characterization and thermal modelling of friction welded alumina-mild steel with the use of Al 1100 interlayer. J Alloys Compd 2010;506(2):703–9. https://doi.org/10.1016/j.jallcom.2010.07.047.

[76] Bouarroudj E, Bouzidi W, Menchic O, Abdid S. Effects of copper powder insert layer on the properties of friction welded joints between AlCu and AISI 4140 structural steel. Defect Diffusion Forum 2009;283–286:166–70. https://doi.org/10.4028/www.scientific.net/DDF.283-286.166.

[77] Madhusudhan Reddy G, Sambasiva Rao A, Mohandas T. Role of electroplated interlayer in continuous drive friction welding of AA6061 to AISI 304 dissimilar metals. Sci Technol Weld 2008;13(7):619–28. https://doi.org/10.1179/174329308X319217.

[78] Dang Z, Qin G, Ma H. Interfacial microstructural characterization and mechanical properties of inertia friction welding of 2219 aluminum alloy to 304 stainless steel. Mater Sci Eng 2021;822. https://doi.org/10.1016/j.msea.2021.141689.

[79] Kawai G, Ogawa K, Ochi H, Tokisue H. Friction weldability of aluminum alloys to carbon steel. J Light Met Weld Constr. 1999;37(7):1–8. https://doi.org/10.1080/09507110009549147.

[80] Fukumoto S, Tsubakino H, Aritoshi M, Tomita T, Okita K. Dynamic recrystallisation phenomena of commercial purity aluminium during friction welding. J Mater Sci Technol 2002;18(2):219–25. https://doi.org/10.1179/026708301225000635.

[81] Kimura M, Ishii H, Kusaka M, Kaizu K, Fuji A. Joining phenomena and joint strength of friction welded joint between pure aluminium and low carbon steel. Sci Technol Weld 2009;14(5):388–95. https://doi.org/10.1179/136217109X425856.

[82] Kimura M, Kusumoto Y, Kusaka M, Kaizu K. Improving the tensile strength between pure al and low carbon steel joint fabricated by friction welding. J Mater Eng Perform 2023;32(10):4655–67. https://doi.org/10.1007/s11665-022-07396-x.

[83] Reddy AC. Fatigue life prediction of different joint designs for friction welding of 1050 mild steel and 1050 aluminum. Int J Sci Eng 2015;6(4):408–12.

[84] Kimura M, Suzuki K, Kusaka M, Kaizu K. Effect of friction welding condition on joining phenomena, tensile strength, and bend ductility of friction welded joint between pure aluminium and aisi 304 stainless steel. J Manuf Process 2017;25:116–25. https://doi.org/10.1016/j.jmapro.2016.12.001.

[85] Kobayashi A, Shigematsu I. Friction welding characteristics of A1070 and SUS304. In: Fujii H, editor. Proceedings of the 1st international joint symposium on joining and welding. Woodhead Publishing; 2013. p. 207–12.

[86] Dang Z, Qin G, Zhao Y, Wang J. Effect of thermo-mechanical distribution on the evolution of imcs layer and mechanical properties of 2219 aluminum alloy/304 stainless steel joints by inertia friction welding. J Mater Res Technol 2022;21:2215–27. https://doi.org/10.1016/j.jmrt.2022.10.054.

[87] Dang Z, Qin G, Wang J. Bonding mechanism and fracture behavior of inertia friction welded joint of 2219 aluminum alloy to 304 stainless steel. Mater Sci Eng A 2023;866:144641. https://doi.org/10.1016/j.msea.2023.144641.

[88] Mullo JL, Ramos-Grez JA, Barrionuevo GO. Effect of laser heat treatment on the mechanical performance and microstructural evolution of AISI 1045 steel-2017-T4 aluminum alloy joints during rotary friction welding. J Mater Eng Perform 2021;30(4):2617–31. https://doi.org/10.1007/s11665-021-05614-6.
[89] Barrionuevo GO, Mullo JL, Ramos-Grez JA. Predicting the ultimate tensile strength of AISI 1045 steel and 2017-T4 aluminum alloy joints in a laser-assisted rotary friction welding process using machine learning: a comparison with response surface methodology. Int J Adv Manuf Technol 2021;116(3–4):1247–57. https://doi.org/10.1007/s00170-021-07469-6.
[90] Wang H, Qin G, Li C. Effect of different friction coefficient models on numerical simulation of inertia friction welding of 2219 Al alloy to 304 stainless steel. J Mater Res Technol 2023;27:6474–83. https://doi.org/10.1016/j.jmrt.2023.11.079.
[91] Fukumoto S, Tsubakino H, Okita K, Aritoshi M, Tomita T. Amorphization by friction welding between 5052 aluminum alloy and 304 stainless steel. Scr Mater 2000;42(8). https://doi.org/10.1016/S1359-6462(00)00299-2.
[92] Dong H, Li Y, Li P, Hao X, Xia Y, Yang G. Inhomogeneous microstructure and mechanical properties of rotary friction welded joints between 5052 aluminum alloy and 304 stainless steel. J Mater Process Technol 2019;272:17–27. https://doi.org/10.1016/j.jmatprotec.2019.04.039.
[93] Lee WB, Yeon Y, Kim D, Jung S. Effect of friction welding parameters on mechanical and metallurgical properties of aluminium alloy 5052–A36 steel joint. J Mater Sci Technol 2003;19(6):773–8. https://doi.org/10.1179/026708303225001876.
[94] Ikeuchi K, Takahashi M, Watanabe H, Aritushi M. Effects of carbon content on intermetallic compound layer and joint strength in friction welding of Al alloy to steel. Weld World 2009;53(5–6):R135–9. https://doi.org/10.1007/BF03266718.
[95] Kimura M, Kusaka M, Kaizu K, Nakata K, Nagatsuka K. Friction welding technique and joint properties of thin-walled pipe friction-welded joint between type 6063 aluminum alloy and aisi 304 austenitic stainless steel. Int J Adv Manuf Technol 2016;82(1–4):489–99. https://doi.org/10.1007/s00170-015-7384-8.
[96] Liu Y, Zhao H, Peng Y, Ma X. Microstructure and tensile strength of aluminum/stainless steel joint welded by inertia friction and continuous drive friction. Weld World 2020. https://doi.org/10.1007/s40194-020-00960-w.
[97] Gotawala N, Shrivastava A. Investigation of interface microstructure and mechanical properties of rotatory friction welded dissimilar aluminum-steel joints. Mater Sci Eng A 2021;825:141900. https://doi.org/10.1016/j.msea.2021.141900.
[98] Hincapié OD, Salazar JA, Restrepo JJ, Graciano-Uribe JA, Torres EA. Weldability of aluminum-steel joints using continuous drive friction welding process, without the presence of intermetallic compounds. Eng J 2020;24(1):129–44. https://doi.org/10.4186/ej.2020.24.1.129.
[99] Ma H, Qin G, Geng P, Wang S, Zhang D. Microstructural characterisation and corrosion behaviour of aluminium alloy/steel hybrid structure produced by friction welding. J Manuf Process 2021;61:349–56. https://doi.org/10.1016/j.jmapro.2020.11.014.
[100] Heppner E, Sasaki T, Trommer F, Woschke E. Model development for numerical analysis of the bonding strength for friction welded lightweight structures. Finite Elem Anal Des 2024;229:104063. https://doi.org/10.1016/j.finel.2023.104063.
[101] Ashfaq M, Sajja N, Khalid Rafi H, Prasad Rao K. Improving strength of stainless steel/aluminum alloy friction welds by modifying faying surface design. J Mater Eng Perform 2013;22(2):376–83. https://doi.org/10.1007/s11665-012-0278-0.
[102] Ma H, Qin G, Dang Z, Geng P. Interfacial microstructure and property of 6061 aluminium alloy/stainless steel hybrid inertia friction welded joint with different steel surface roughness. Mater Charact 2021;179. https://doi.org/10.1016/j.matchar.2021.111347.
[103] Kimura M, Sakino S, Kusaka M, Kaizu K, Hayashida K. Characteristics of friction welded joint between 6063 aluminum alloy and AISI 304 stainless steel through post-weld heat treatment. J Manuf Process 2020;58:302–10. https://doi.org/10.1016/j.jmapro.2020.08.003.
[104] Kannan P, Balamurgan K, Thirunavukkarasu K, Sreenivasan M. Behaviour of dissimilar friction welds with the introduction of silver interlayer. Appl Mech Mater 2012;224:178–83. https://doi.org/10.4028/www.scientific.net/AMM.224.178.
[105] Senthil Murugan S, Sathiya P, Noorul Haq A. Experimental study on the effect of silver, nickel and chromium interlayers and upset pressure in joining SS304L-AA6063 alloys through direct drive friction welding process. J Braz Soc Mech Sci Eng 2020;42(11). https://doi.org/10.1007/s40430-020-02687-7.
[106] Kimura M, Yukawa T, Kusaka M, Kaizu K, Fuji A. Possibility of direct friction welding between type 7075 aluminum alloy and low carbon steel. In: Fujii H, editor. Proceedings of the 1st international joint symposium on joining and welding. Woodhead Publishing; 2013. p. 267–73.
[107] Gupta J, Bhardwaj B, Sharma V, editors. Friction welding process of AA7075 aluminium alloy to mild steel. Recent Innovations in Mechanical Engineering. Singapore: Springer Singapore; 2022. 2022//.
[108] Microstructure and residual stress in rotary friction welded dissimilar metals of AA7020 aluminium alloy with 316L steel. In: Gan WM, Hofmann M, Ventzke V, Randau C, Huang YD, Kriele A, et al., editors. Mater sci forum. Trans Tech Publ; 2017.
[109] Multilayer perceptron tutorial. In: Noriega L, editor. School of computing. Staffordshire University; 2005.
[110] Mirzadeh H, Najafizadeh A. Modeling the reversion of martensite in the cold worked AISI 304 stainless steel by artificial neural networks. Mater Des 2009;30(3):570–3. https://doi.org/10.1016/j.matdes.2008.05.057.
[111] Darvazi AR, Iranmanesh M. Prediction of asymmetric transient temperature and longitudinal residual stress in friction stir welding of 304L stainless steel. Mater Des 2014;55:812–20. https://doi.org/10.1016/j.matdes.2013.10.030.
[112] Li W, Shi S, Wang F, Zhang Z, Ma T, Li J. Numerical simulation of friction welding processes based on abaqus environment. J Eng Sci Technol Rev 2012;5(3). https://doi.org/10.25103/jestr.053.03.
[113] Sadeghian B, Taherizadeh A, Atapour M, Saeidi N, Alhaji A. Phase-field simulation of microstructure evolution during friction stir welding of 304 stainless steel. Mech Mater 2021;163:104076. https://doi.org/10.1016/j.mechmat.2021.104076.
[114] Sadeghian B, Taherizadeh A, Atapour M. Simulation of weld morphology during friction stir welding of aluminum-stainless steel joint. J Mater Process Technol 2018;259:96–108. https://doi.org/10.1016/j.jmatprotec.2018.04.012.

My research focuses on the following areas: 1-Hydrogen Production and Embrittlement in Steel, Ni-based Alloys, etc. 2- Hydrogen production 3-Microstructure-Process-Property Relationships, with a particular emphasis on grain boundary engineering. 4-High-Performance Metal Matrix Composites (MMCs). 5-Smart Dry Mechanical Powder Processing. 6- Hydrogen-based direct reduction of iron oxide, 7- Solid -state joining suchas Friction stir welding, Friction spot stir welding. Current Position: Assistant professor in department of engineering at Salento university, Italy Research Focus: Green hydrogen, Hydrogen embrittlement, Direct reduction of iron oxide, High Performance MMCs, Grain boundary engineering Publications: Please see my Googlescholar or ResearcGate page. https://www.researchgate.net/profile/Behzad-Sadeghi/research?ev=prf_act&_tp=eyJjb250ZXh0Ijp7ImZpcnN0UGFnZSI6ImhvbWUiLCJwYWdlIjoicHJvZmlsZSIsInByZXZpb3VzUGFnZSI6ImhvbWUiLCJwb3NpdGlvbiI6InBhZ2VIZWFkZXIifX0